

RESEARCH ARTICLE Direct measurements of wind stress over the surf zone

10.1002/2013JC009585

Behnam Shabani¹, Peter Nielsen¹, and Tom Baldock¹¹School of Civil Engineering, University of Queensland, Brisbane, Queensland, Australia

Key Points:

- A new field data set of the wind stress over surf zone waves is presented
- Concept of an apparent wave steepness is proposed to explain drag observations
- Surf zone drag coefficients were almost twice the values outside the surf

Correspondence to:

B. Shabani,
b.shabani@uq.edu.au

Citation:

Shabani, B., P. Nielsen, and T. Baldock (2014), Direct measurements of wind stress over the surf zone, *J. Geophys. Res. Oceans*, 119, 2949–2973, doi:10.1002/2013JC009585.

Received 6 NOV 2013

Accepted 23 APR 2014

Accepted article online 28 APR 2014

Published online 14 MAY 2014

Abstract Field data of the wind stress over surf zone waves are presented from an open ocean beach on the East Australian Coast. Two ultrasonic anemometers were deployed at nominal heights of 5 and 10 m above the water surface in the intertidal and inner surf zones, with concurrent measurements of water levels and offshore wave parameters. Following a rigorous quality control procedure, the wind stress was determined by the eddy correlation technique. A constant stress layer was observed between 5 and 10 m elevation. Considering near-neutral conditions only, the wind drag coefficients were found to systematically change with the wind angle of approach relative to the shoreline and are much smaller for longshore wind than during onshore wind. The concept of an apparent wave steepness changing with wind direction is suggested to explain this behavior. The drag coefficients over the surf zone during onshore wind and near-neutral conditions were determined to be almost twice the values expected at the same wind speed and open ocean conditions. The observed Charnock coefficient was similarly an order of magnitude larger than open ocean values. A wave celerity of the order of that expected in the inner surf zone is required to explain the observed large roughness and drag coefficients using existing wave age-dependent parameterizations. This suggests that the slower wave celerity in the surf zone is an important contributor to the increased wind stress, in addition to the sawtooth wave shape.

1. Introduction

The momentum transferred into the ocean through the wind shear stress on the ocean surface contributes toward generating wind waves, driving ocean currents, and raising the mean water level through storm surges. The magnitude of the wind shear stress and drag coefficient is therefore critical for modeling storm surge wind setup. The wind setup is inversely proportional to the water depth, and therefore a large part of the wind setup occurs in shallow water, especially across the surf zone [Walton and Dean, 2009]. However, limited data exist from the nearshore region and surf zone, and models typically utilize wind drag coefficients obtained from measurements over the deep ocean. Letchford and Zachry [2009], for instance, point out that the ADCIRC hydrodynamic model uses the linear drag coefficient formulation of Garratt [1977], which is an open ocean formula, as the default value. Tang et al. [1997], Lentz et al. [1999], and Reniers et al. [2004] also adopted open ocean drag coefficients in their modeling.

With analogy to the wind flow over a solid surface, evaluating the wind shear stress (τ) on the ocean surface is equivalent to finding the wind drag coefficient (C_D) or alternatively the aerodynamic roughness of the ocean surface (z_0). Wind flow over the ocean, however, is a more complex problem to address than flow over solid boundaries. The complexity is partly attributed to the variety of atmospheric and oceanic parameters which may influence the air-sea interaction. This includes wind speed, atmospheric stability, wave height, wave length, wave celerity, sea-spray effects, wave breaking and shoaling processes, etc. At the same time, an interdependency also exists between the two mediums, given that ocean waves (roughness elements) are themselves products of the overhead wind flow. Experimental and field data are therefore essential to successfully estimate and parameterize the wind drag coefficient over the ocean surface.

Despite some disagreements in early studies, it is now widely accepted that the wind drag coefficient increases with wind speed [Smith and Banke, 1975]. Two forms of the variation of the drag coefficient versus wind speed have been frequently suggested throughout the literature. This includes the widely used Charnock [1955] relationship where the aerodynamic roughness of the ocean surface is parameterized as

$$z_0 = \alpha \frac{U_*^2}{g} \quad (1)$$

in which u_* is the shear velocity, g is the gravitational acceleration, and α is the Charnock coefficient. The proposed dependency between the roughness (z_0) and the shear velocity (u_*) also implies that the drag coefficient (C_D) increases monotonically with increasing wind velocity (\bar{u}). Different experimental values of the Charnock coefficient have been proposed, mostly in the range of $\alpha=0.01-0.02$ [Wu, 1969; Hicks, 1972; Smith and Banke, 1975; Garratt, 1977; Smith, 1980; Wu, 1980; Geernaert et al., 1986; Johnson et al., 1998]. Another form of parameterization, suggesting a linear increase of the drag coefficient versus wind speed ($C_D=a\bar{u}+b$), has also been frequently proposed [Smith, 1973, 1974; Smith and Banke, 1975; Garratt, 1977; Smith, 1980; Wu, 1980; Large and Pond, 1981; Geernaert et al., 1986, 1987; Smith et al., 1992; Yelland and Taylor, 1996; Vickers and Mahrt, 1997a; Drennan et al., 1999; Oost et al., 2002].

The wind speed dependency of the drag coefficient reflects the interdependency between wind and waves. That is, those waves acting as roughness elements grow as the wind speed increases. However, a unique set of empirical coefficients a and b , or alternatively α , has not been found since the wave conditions are also controlled by other independent parameters such as the wind fetch, wind duration, water depth, and shoaling effects on wave properties including the wave shape and celerity, etc. A wind speed-dependent parameterization should therefore be at least accompanied by a constraint on sea state parameters—e.g., open ocean conditions. Similarly, additional processes such as the generation of sea-spray and foam patches and enhanced wave breaking take effect in the storm-scale range of wind speeds. As a result, the linear and Charnock-type parameterizations are not valid under these circumstances. This was demonstrated for the first time in the light of recent field and laboratory measurements by Powell et al. [2003], Donelan et al. [2004], Black et al. [2007], Jarosz et al. [2007], and Zachry et al. [2009] where the wind drag coefficient was found to level off at around $C_D=0.0020-0.0025$ when the wind speed exceeds a threshold between 23–40 m/s. It may be noted though that an agreement has not yet been reached on the role of additional processes such as sea-spray effects on the drag behavior during high wind speeds. Recently, Andreas et al. [2012] suggested a new wind shear stress parameterization in the form of a linear relationship between the wind shear velocity (u_*) and the wind speed (\bar{u}). The parameterization is capable of producing a role off in the drag coefficient during high wind speeds without the need for activating additional processes such as spray effects.

The idea of the sea state dependency of the aerodynamic roughness was first hypothesized by Kitaigorodskii and Volkov [1965] and promoted by others such as Stewart [1974]. On this basis, the wind drag coefficient is suggested to reduce as seas become older, i.e., by increasing the wave age (c_p/u_*) where c_p is the wave celerity corresponding to the wave spectrum peak. In other words, the wind drag coefficient is larger over actively growing young waves than over fully developed mature seas. Several forms of sea state-dependent parameterization are currently suggested to express the effects of the wave field on the aerodynamic roughness and wind drag coefficient over the ocean. In a commonly used form, the Charnock coefficient is expressed as a power function of the wave age parameter, rather than a constant, i.e., $\alpha=a(c_p/u_*)^{-b}$ where a and b are positive numerical coefficients. Field data sets have been used to provide numerical values for the coefficients a and b [Maat et al., 1991; DeCosmo, 1991; Smith et al., 1992; Monbaliu, 1994; Vickers and Mahrt, 1997a; Johnson et al., 1998; Oost et al., 2002; Drennan et al., 2003]. Taylor and Yelland [2001], however, argued that a wave age-dependent parameterization based on one field data set often may not successfully model another set of field data; nor could it bring the laboratory and field data together within a single parameterization. Hence, they suggested a steepness-dependent parameterization as $z_0/H_s=a(H_s/\lambda_p)^b$ where H_s and λ_p are, respectively, the significant wave height and the wavelength corresponding to the wave spectrum peak. Nevertheless, Drennan et al. [2005] compared the wave age and the wave steepness-dependent parameterizations, using several field data sets and concluded that despite improvements by both models, no one model successfully described every data set. Recently, a new parameterization based on the wave length scaling of the roughness and the drag coefficient has been proposed in Hwang [2004, 2005a, 2005b, 2010] and Hwang et al. [2011]. The model suggests to parameterize z_0/λ_p and $C_{D\lambda}$ as power functions of the wind forcing ($\omega_p u_*/g$), i.e., the inverse wave age (u_*/c_p), where ω_p is the peak wave frequency, and $C_{D\lambda}$ is the drag coefficient referenced to $z=\lambda_p$ above the water surface instead of the conventional drag coefficient corresponding to $z=10$ m. This choice is based on the idea that Wave Boundary Layer effects will be almost diminished at the height of $z=\lambda_p$, which may therefore help to reduce variability in drag parameterizations. Nevertheless, Andreas [2009] raised concern about a potential fictitious correlation in this type of parameterization.

As the review above indicates, the wind drag coefficient over the ocean has been subject to extensive research for several decades. However, given the interest in the problem of wind wave generation, the focus was primarily on deep water. Sea state-dependent parameterizations of the drag coefficient were suggested as a means to overcome the variabilities observed among different data sets. This subsequently led to an interest in measurements over shallower regions of the ocean (15–50 m). This was because the measurements in shallow water widens the range of wave celerity and thus wave age values, allowing more reliable wave age-dependent parameterizations to be developed. This is in particular useful for modeling scenarios where waves are in their early stages of development, i.e., when they are young. With this objective, the regions with strong wave shoaling were often avoided to prevent contamination of data. Likewise, breaking waves were also avoided for the same reason. Despite good progress, especially since 1990s, work is still required in shallow water to explain differences between different data sets and parameterizations [cf., *Drennan et al.*, 2005], and additional variables and physical processes need to be investigated and incorporated in drag coefficient parameterizations [*Babanin and Makin*, 2008]. *Smith et al.* [1996] discussed the progress made in air-sea interaction studies and stated that they expect future data sets to be collected in coastal regions where depth and fetch influence the waves and the fluxes, to cover events which contain large gradients and to validate modeling and understanding of extreme events. Since then, an area which has remained largely unexplored is the wind stress over coastal water, and in particular the surf zone.

Recently, *Zachry et al.* [2009] collected wind stress data using the *Turbulent Intensity* (TI) method in a coastal area during Hurricane Ike. Measured drag coefficients increased very slowly with the wind speed, in comparison with the open ocean data. At high wind speed, the data were quite similar to open ocean drag coefficients, but at low and moderate speeds, they were much larger than deep water values. However, there were uncertainties due to potential *Internal Boundary Layer* (IBL) effects arising from the exposure of the land between the waterline and the measurement point, during low and moderate wind speed, especially given the low measurement height of only about 2 m above the ground and the long 90 m land fetch at full waterline recession. At high wind speed during the peak of the event, nevertheless, the measurement point was drowned, thus avoiding potential contamination by IBL effects. On the other hand, *Vickers and Mahrt* [2010] recently suggested that the aerodynamic roughness in the coastal zone is smaller than those given by widely used open ocean models during weak and moderate winds. Roughness values in the coastal zone, however, were similar to the open ocean values during high wind speeds. It should be mentioned though that the data sets used in *Vickers and Mahrt* [2010] (aircraft data during the CBLAST and SHOWEX experiments) were observations over shallow water and not the surf zone.

Thus, the wind stress on the surf zone has remained largely unexplored, and differences are expected since waves in the surf zone and surrounding coastal water travel with much slower speeds than deep water waves. At the same time, surf zone waves exhibit different shapes from the waves in other regions of the ocean. The present study addresses this issue and presents a new data set from full-scale field experiments to investigate the wind shear stress on the surf zone and surrounding coastal water using the direct method—or eddy correlation technique. The paper is organized as follows: the theoretical background required to analyze and explain the data is described in the next section, followed by a description of the field study, including the field site, instrumentations, and measurements. An overview of the data analysis and quality controls is then presented, before presenting the results of the field experiment. A discussion and summary of the results conclude the paper.

2. Theoretical Background

The Reynolds shear stress (τ_t), or the turbulent flux of momentum, at a given elevation above the ocean surface is defined as

$$\tau_t = -\rho_a \overline{u'w'} \quad (2)$$

where ρ_a is the air density; u and w are, respectively, horizontal and vertical components of instantaneous wind velocity at that elevation; the prime symbol denotes turbulent fluctuations of a quantity relative to its

mean value, e.g., $u' = u - \bar{u}$; and the overbar indicates time-averaging over a suitable period. Note that a positive flux (τ_t) implies a downward transfer of horizontal momentum. Near the boundary (ocean) surface, additional mechanisms such as viscous effects, wave-induced air motions, and spray-induced effects also contribute to the total wind shear stress (τ). Away from these near-surface mechanisms, however, the wind shear stress is expected to be entirely due to the turbulence, so that $\tau = \tau_t$. Following the assumption of a constant shear stress layer, one may consider τ at its measurement height to have the same value as the shear stress at the boundary surface (τ_0). The surface flux of momentum is often expressed in the form of a wind shear velocity (u_*) as

$$\tau_0 = \rho_a u_*^2 \tag{3}$$

The shear velocity is a scaling parameter for the vertical gradient of the mean wind speed and is used to scale the following universal function proposed in Monin-Obukhov similarity theory

$$\frac{\partial \bar{u}}{\partial z} = \frac{u_*}{\kappa z} \phi_m \left(\frac{z}{L} \right) \tag{4}$$

in which z is the elevation measured positive upward from the boundary surface and κ is the von-Karman constant. The nondimensional velocity gradient function ϕ_m is a function of the stability parameter (z/L), where L is the Monin-Obukhov length scale defined as

$$L = - \frac{u_*^3 \bar{\theta}_v}{g \kappa \theta'_v w'} \tag{5}$$

in which $\bar{\theta}_v$ is the mean virtual temperature of air, θ'_v represents the fluctuations of the virtual temperature, and g is the gravitational acceleration. Equation (4) provides the vertical distribution of the mean wind speed, once integrated from the roughness height z_0 to the elevation z ,

$$\bar{u} = \frac{u_*}{\kappa} \left[\ln \frac{z}{z_0} - \psi_m \left(\frac{z}{L} \right) \right] \tag{6}$$

where ψ_m is the stability function corresponding to the momentum flux and is the integrated form of the gradient function (ϕ_m).

Under neutral atmospheric stability conditions, equations (4) and (6) reduce to the well-known logarithmic wind velocity profile

$$\frac{\partial \bar{u}}{\partial z} = \frac{u_*}{\kappa z} \tag{7}$$

$$\bar{u} = \frac{u_*}{\kappa} \ln \frac{z}{z_0} \tag{8}$$

The nondimensional velocity gradient (ϕ_m) and the stability function (ψ_m) alter the velocity profile from the logarithmic distribution according the local stability condition described by the stability parameter (z/L). A widely used form of the gradient function is the *Businger et al.* [1971] representation

$$\phi_m \left(\frac{z}{L} \right) = \left(1 - \alpha_b \frac{z}{L} \right)^{-\frac{1}{4}} \quad \text{when } \frac{z}{L} < 0 \tag{9}$$

$$\phi_m \left(\frac{z}{L} \right) = 1 + \beta_b \frac{z}{L} \quad \text{when } \frac{z}{L} > 0 \tag{10}$$

The set of values $\alpha_b = 20$, $\beta_b = 5$, and $\kappa = 0.4$ is used here, as in *Yelland and Taylor* [1996]. Following *Paulson* [1970], the stability function (ψ_m) during unstable conditions is expressed as

$$\psi_m\left(\frac{z}{L}\right) = 2\ln\left(\frac{1+\phi_m^{-1}}{2}\right) + \ln\left(\frac{1+\phi_m^{-2}}{2}\right) - 2\tan^{-1}(\phi_m^{-1}) + \frac{\pi}{2} \quad \text{when } \frac{z}{L} \leq 0 \tag{11}$$

and according to *Lo and McBean* [1978] during stable conditions

$$\psi_m\left(\frac{z}{L}\right) = 1 - \phi_m \quad \text{when } \frac{z}{L} \geq 0 \tag{12}$$

The wind shear stress is often expressed in terms of a wind drag coefficient (C_{Dz}) through the conventional relationships

$$C_{Dz} = \frac{\tau_o}{\rho_a \bar{u}_z^2} \tag{13}$$

$$C_{Dz} = \left(\frac{u_*}{\bar{u}_z}\right)^2 \tag{14}$$

where \bar{u}_z is the mean wind speed at height z above the sea surface. Typically, \bar{u}_{10} is used for this purpose.

The vertical profile of the wind velocity is dependent on the local stability conditions as described by equations (4) and (6). The effect of the stability on the drag coefficient is represented by the stability-dependent \bar{u}_z in equations (13) and (14). In order to compare the drag coefficients measured under different stability conditions with each other, the stability effects should be accounted for to report the equivalent drag coefficient under neutral stability conditions. The neutral-equivalent drag coefficient (C_{DNz}) is simply defined based on the mean wind speed under the neutral stability conditions (\bar{u}_{Nz}) as

$$C_{DNz} = \frac{\tau_o}{\rho_a \bar{u}_{Nz}^2} \tag{15}$$

The neutral wind speed (\bar{u}_{Nz}) is obtained from equation (8). Using the general form of the wind velocity profile in equation (6) and that under neutral stability conditions in equation (8), C_{DNz} and C_{Dz} can be related to each other as

$$C_{DNz} = \left[C_{Dz}^{-\frac{1}{2}} + \frac{\psi_m\left(\frac{z}{L}\right)}{\kappa} \right]^{-2} \tag{16}$$

The wind measurements may not necessarily be taken at the 10 m elevation. However, it is customary to report the drag coefficient with reference to the 10 m wind velocity in order to make various measurements comparable with one another. For this purpose, the wind velocity profile in equation (8) can be used to express the wind velocities at any two elevations such as z_1 and z_2 in terms of each other, with z_2 taken as 10 m for the present study. Similarly, the drag coefficients that are referenced to the wind velocity at these two elevations can also be correlated with each other

$$\frac{C_{DNz_2}}{C_{DNz_1}} = \left(\frac{\bar{u}_{Nz_1}}{\bar{u}_{Nz_2}}\right)^2 = \left(\frac{\ln\frac{z_1}{z_o}}{\ln\frac{z_2}{z_o}}\right)^2 \tag{17}$$

3. Field Site

The field site was located at Main Beach near Point Lookout, North Stradbroke Island, Australia. The western side of the island is bound by the Moreton Bay, which separates the island from the Australian Mainland. The eastern side of the island, where the field site was located, is open to South Pacific Ocean via the Coral Sea. The site locality and a close-up view of the field site are shown in Figure 1. Wind stress measurements

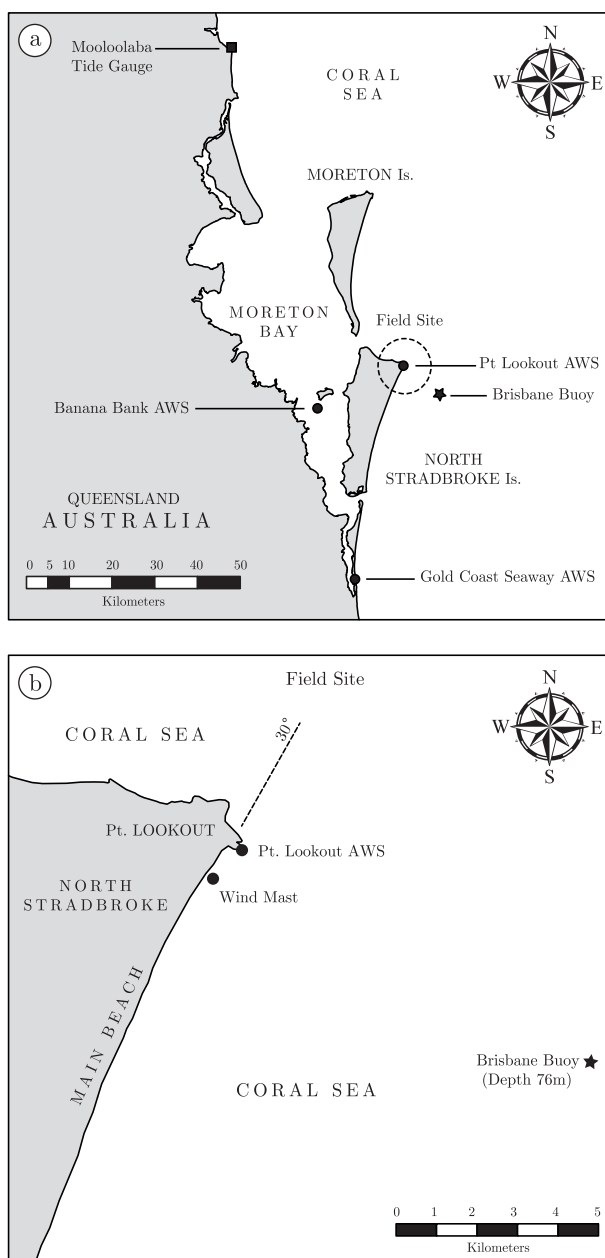


Figure 1. The field site during the Stradbroke 2012 field campaign: (a) the site locality, (b) a close-up view of the site. Third-party tide, wave, and weather monitoring stations are also marked on the figure.

76 m. The buoy is located at $27^{\circ}29'17.10''S$ and $153^{\circ}37'55.86''E$ and provides the following offshore wave information: significant wave height (H_{os}), maximum wave height ($H_{o\ max}$), and mean wave period (T_2) all based on the zero up-crossing method, as well as the peak wave period (T_p), peak wave direction (α_{op}), and sea surface temperature (θ_{osea}). Wave parameters are evaluated over 26.62 min long records and reported at 30 min intervals. The Mooloolaba tide gauge located at $26^{\circ}41'08.40''S$ and $153^{\circ}07'57.60''E$ provides mean water level measurements inside the Mooloolaba river entrance at 10 min intervals. Measured data represent offshore mean water levels since no or very little wave setup is expected to occur in the river entrance as suggested by Hanslow and Nielsen [1992] and Dunn [2003]. There are also a number of automatic weather stations (AWS) surrounding the field site providing observations of the mean wind speed, mean wind direction, rainfall, etc. The mean wind speed and direction from weather stations are used to cross-check wind measurements during the present study. The rainfall status is also an important parameter for the purpose of

during the field campaign were carried out on a wind mast deployed at $27^{\circ}26'35.70''S$ and $153^{\circ}32'18.70''E$. The location of the wind mast is also marked on the figure. The beach orientation at the field site is along 30° clockwise from the North and is therefore oriented favorably for the dominant South-Easterly winds.

The *North Stradbroke 2012 Field Campaign* was a month-long intensive experiment from 4 May 2012 to 1 June 2012. Measurements during this period were mostly continuous and interrupted only for about an hour on each day for power supply replacement and data retrieval. Measured parameters during this period include high-frequency three-dimensional wind velocities and sonic air temperature at different elevations, nearshore wave, and water level, including at the wind mast location, water temperature, shoreline location, daily beach sand level profiles, etc. At the same time, third-party institutions operate monitoring stations at nearby locations as part of the Australian national monitoring network. This includes wave buoys, tide gauges, and automatic weather stations (AWS). The locations of some third-party monitoring stations have also been shown in Figure 1. In particular, the Brisbane wave buoy provides offshore wave measurements from a 0.9 m Waverider buoy located just offshore the field site at a water depth of

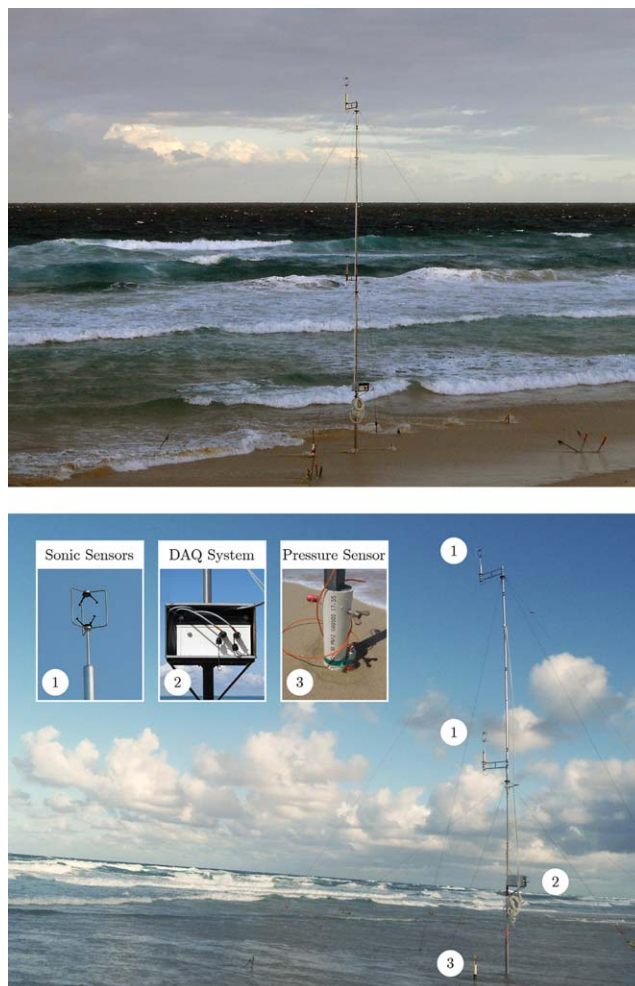


Figure 2. The wind mast during the Stradbroke 2012 field campaign. (1) The location of ultrasonic anemometers, (2) the data acquisition (DAQ) system, and (3) the water level sensor has been marked in the lower photograph.

base of the wind mast to obtain instantaneous water level measurements. The locations of ultrasonic anemometers, the data acquisition system, and the water level sensor have been marked on the lower photograph in Figure 2.

The wind mast was designed to be set up in shallow parts of the inner surf zone. The design allows wind measurements to be made while the wind mast is located inside the water or very close to the shoreline. As a result, the wind runs no, or only a very short, distance on the sandy beach before reaching the wind mast. It should be noted that an internal wind boundary layer forms when the wind departs the water surface onto the sandy beach, and it grows thicker as the wind travels further on the beach face [Shabani, 2014]. The internal boundary layer may eventually reach the elevation of anemometers and influence their measurements if the wind mast is located a considerable distance landward of the shoreline. Here the wind mast was deployed very close to the shoreline in order to avoid such internal boundary layer effects (cf. Figure 2).

The cross-shore distance between the wind mast and the shoreline ($x_{shoreline}$) is measured due to its importance in identifying the status of the internal boundary layer over the sandy beach. For this purpose, the shoreline is defined as the location where the mean water surface intersects the beach sand level. This is a point within the swash zone and can be visually identified as the interface between the glossy and matt surfaces observed on the sandy beach. In the present study, the shoreline location is visually identified and manually measured relative to the wind mast location at 15 min intervals. Nevertheless, field measurements are carried out on a 24 h basis but are only manned during the daytime. An alternative method is therefore

data quality control. The closest weather station was located at Point Lookout, about 1 km away from the field site.

4. Instrumentations and Measurements

4.1. Wind Mast

A 10 m high guyed wind mast (Figure 2) was deployed in order to carry out the wind stress measurement. The slim body of the wind mast, which is 40 mm in diameter, imposes minimal flow disturbances on the wind stress measurements. A wind tunnel test showed that the flow disturbances at a wind speed of 10 m/s are confined within a radius of 30 cm from the wind mast, approximately 8 times the mast diameter. Flow disturbances were avoided by using brackets enabling the sensors to be mounted about 60 cm away from the mast body. Wind measurements were carried using two ultrasonic anemometers mounted at 6.9 and 11.9 mAH (Rel. to the Australian Height Datum) on the wind mast. At the base of the mast, the mean water level (MWL) and the sand level varied within the range of 0.6–1.4 mAH during the deployment period. A pressure transducer was mounted at the

used to evaluate the shoreline location during unmanned data collection periods. Based on the empirical relationship of D. J. Hanslow and P. Nielsen (special issue on Shoreline set-up on natural beaches, *J. Coastal Res.*, 15, 1–10 pp., 1993), the wave setup at the shoreline is estimated to be $0.38H_{orms}$ where H_{orms} is the offshore RMS wave height. On this basis, the shoreline elevation ($z_{shoreline}$) is expressed as

$$z_{shoreline} = z_{omwl} + 0.38H_{orms} \tag{18}$$

in which z_{omwl} is the offshore mean water level. The offshore wave height is measured at the Brisbane wave buoy located just offshore the field site, while the offshore mean water level is available from the Mooloolaba tide gauge. The cross-shore profile of the beach sand level was surveyed on a daily basis during the present study. The cross-shore sand level profile and the shoreline elevation ($z_{shoreline}$) are used together to obtain the shoreline location ($x_{shoreline}$) relative to the wind mast. $x_{shoreline}$ is defined as positive when the shoreline is located seaward of the wind mast. The predicted shoreline location using equation (18) is found to be in very good agreement with manual measurements during manned data collection periods, i.e., often within 5 or at most 10 m distance from each other. Equation (18) can therefore be reliably used to predict the shoreline location during unmanned periods.

The time series of the shoreline location during the field campaign is plotted in Figure 3. The upper horizontal axis shows the local time and date based on the Australian Eastern Standard Time (AEST). The time series

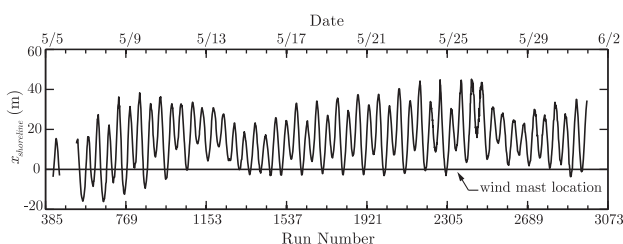


Figure 3. The cross-shore distance ($x_{shoreline}$) between the shoreline and the wind mast during the field experiment. $x_{shoreline}$ is positive when the shoreline is located seaward of the wind mast. Equation (18) is used to evaluate the shoreline location.

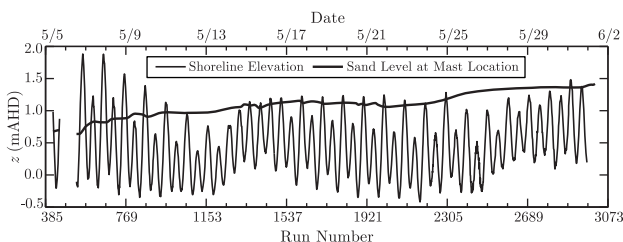


Figure 4. The shoreline elevation ($z_{shoreline}$) during the field experiment. Equation (18) is used to evaluate the shoreline location. The thick solid line corresponds to the surveyed sand level at the wind mast location.

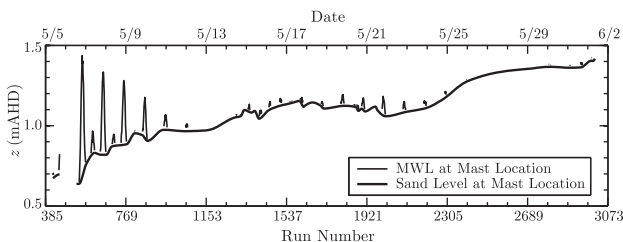


Figure 5. The mean water level at the wind mast location measured by a pressure sensor during the field experiment. The thick solid line corresponds to the surveyed sand level at the mast location.

of data is split into smaller blocks referred to as Data Runs. Each run is assigned a Run Number, starting from “1” for the data run beginning on 1 May 2012 00:00:00 and continuing consecutively at 15 min intervals. Each data run contains 15 min of field data. The same numbering arrangement is used for all other types of data collected or used during the present field campaign. Corresponding run numbers are shown on the lower horizontal axis in Figure 3. The wind mast is located at $x_{shoreline} = 0$. As shown, the shoreline is at the wind mast location (or landward of the wind mast) during the high tide on most days. The exposed sandy beach between the wind mast and the shoreline reaches at most 40 m in length during the low tide on some field days. The influence of this is discussed in section 7.1.

The shoreline elevation ($z_{shoreline}$) obtained from equation (18) is plotted in Figure 4. The time series of sand level at the base of the wind mast is also overlaid on the same graph. Note that the wind mast was deployed low on the beach, and the shoreline elevation was considerably higher

than the sand level at the wind mast location during the first few days of the deployment. However, a significant amount of accretion occurred over the course of field campaign, and the sand level at the mast location gradually increased about a meter from 0.5 to nearly 1.5 mAH. This in turn gradually pushed the shoreline further seaward. On subsequent field days, therefore, the wind mast was fully inundated only during the high tide. A pressure transducer (see section 4.3.2) was deployed adjacent to the wind mast in order to obtain instantaneous water level measurements. Figure 5 shows the recorded time series of the mean water level at the base of the wind mast. The greater of the mean water level and the sand level for each data run is taken as the elevation datum for wind drag calculations in the present study. In other words, the mean water level (MWL) is considered the elevation datum when the wind mast is inundated, while the sand level is used for this purpose when the base of the mast is dry. During the early part of field experiment, the mean water depth at the wind mast location reached about 1 m, and the instantaneous water depth was as high as 2 m. Later during the experiment, however, the shoreline gradually receded seaward. During this period, it was mainly wave run-up (swash) surrounding the base of the wind mast.

4.2. Anemometers

Gill Wind Master Pro three-dimensional ultrasonic anemometers were used to measure the wind velocity and sonic temperature, with a sampling rate of 32 Hz. Since the elevation datum for evaluating the wind drag coefficient was taken as the greater of the mean water level and the sand level at the wind mast location, the datum is therefore different for each data run. The two anemometers were, respectively, 5.5–6.3

m and 10.5–11.3 m above these data. These elevations are chosen high enough to ensure that anemometers are outside any internal boundary layer which develops over the sandy beach as the wind departs the ocean. The use of two anemometers allows the assumption of a constant shear stress layer, and any impact of the near-surface mechanisms on this assumption, to be examined.

A Campbell Scientific CR1000 Data Logger was used to record outputs of the ultrasonic anemometers. The time series of the mean wind velocity (\bar{u}) recorded during the field campaign from the upper anemometer is shown in Figure 6. The averaging period used for this purpose is 15 min, i.e., the duration of a data run. The range of mean wind speeds covered during the field experiment was 0–14 m/s. The corresponding time series of the mean wind direction (α_w) is plotted in Figure 7. Cardinal points are marked for reference on the right-hand vertical axis. Note that only those runs with $\bar{u} \geq 3$ m/s are plotted, since the wind direction cannot be evaluated reliably during low

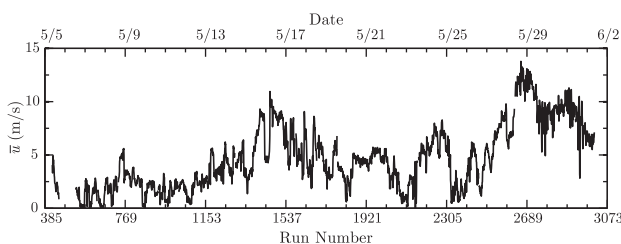


Figure 6. Measured mean wind speed during the field campaign. An averaging period of 15 min has been used. Data are based on measurements from the upper ultrasonic anemometer at 11.9 mAH.

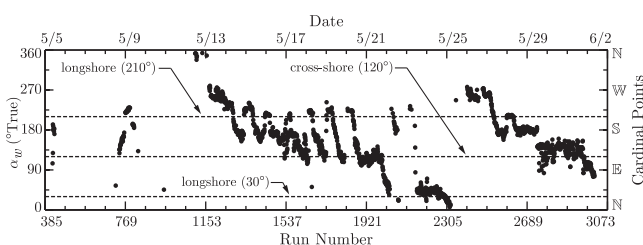


Figure 7. Measured mean wind direction during the field campaign. An averaging period of 15 min has been used. Each data point is the average of mean wind directions measured by lower and upper anemometers. Wind direction data are plotted only if $\bar{u} \geq 3$ m/s at the upper anemometer.

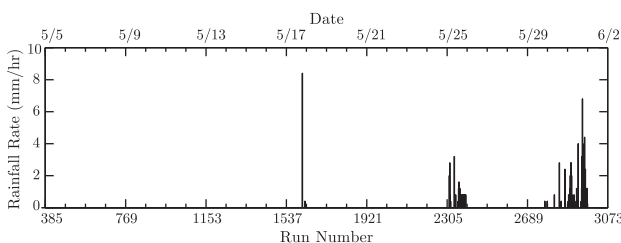


Figure 8. Rainfall intensity during the field campaign.

wind speeds. For reference, the long-shore and cross-shore (onshore) directions are also overlaid as dashed lines in Figure 7.

4.3. Other Measurements

4.3.1. Rainfall Intensity

The rainfall intensity can be important for the reliability of wind stress measurements. On one hand, rain droplets may physically affect the wind shear stress and the wind velocity profile, e.g., by altering the vertical mixing of the horizontal momentum. The authors, however, are unaware of any systematic study on this matter. Despite this, such effects are intuitively expected to be relevant only during very heavy rainfalls. On the other hand, the rain may directly affect wind velocity measurements by disturbing the operation of the ultrasonic anemometers. This can be by rain droplets blocking the sonic path between sonic transducers or as the result of rain water accumulation on the transducer surface. Records of the wind velocity and sonic temperature can be expected to become spiky as a result. Generally speaking, time-averaged quantities such as the mean wind speed and the mean sonic temperature are robust parameters and may only be affected when the rainfall intensity is very high. Turbulent fluxes of momentum, which are calculated based on the covariance of different wind velocity components, however, are not as robust. The rain and the associated spikiness of wind velocity records can therefore introduce errors to measurements of the wind shear stress ($\rho \overline{u'w'}$). The turbulent flux of heat and subsequent atmospheric stability calculations will be similarly affected by the rain. Rainfall data are therefore of interest for the present study and are used during the quality control of wind stress data. They are obtained from observations at nearby weather stations. Figure

8 shows the time series of the rainfall intensity during the field campaign. As shown, it was mostly dry during the field experiment. Otherwise, the rainfall was very light (<2.5 mm/h) or moderate (2.5–7.5 mm/h).

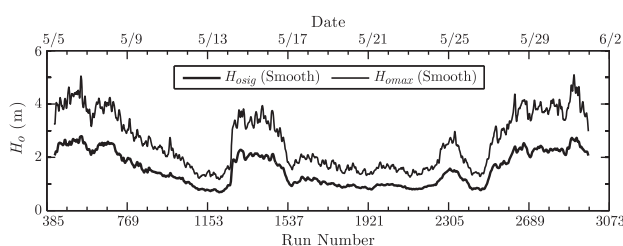


Figure 9. Offshore significant (H_{0sig}) and maximum (H_{0max}) wave heights based on measurements by the Brisbane wave buoy during the field campaign.

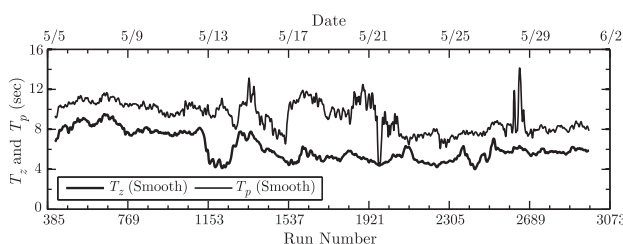


Figure 10. Mean (T_z) and peak (T_p) wave periods based on measurements by the Brisbane wave buoy during the field campaign.

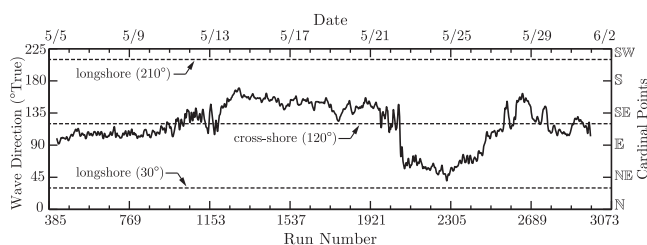


Figure 11. Offshore wave direction based on measurements by the Brisbane wave buoy during the field campaign.

4.3.2. Nearshore Waves, Water Level, and Water Temperature

A pressure transducer was deployed at the location of the wind mast in order to measure the instantaneous water level. Another pressure transducer (or more during some field days) was deployed within the inner surf zone, in a location permanently inside the water, up to 100 m seaward of the wind mast. INW AqiStar PT2X self-logging sensors with a sampling rate of 5 Hz were used for this purpose. The same sensors were also used to measure the water temperature. The intake elevation of each pressure sensor, which was mounted near the seabed surface, was surveyed shortly after the deployment. Recorded surf zone water level data are therefore available referenced to the Australian Height Datum (AHD). A zero-crossing

analysis was also carried out on the measured water level data in order to obtain the surf zone wave height, wave period, and wave shape.

4.3.3. Offshore Wave Climate

Time series of the offshore significant and maximum wave heights (H_{osig} and $H_{o\ max}$), the average zero-crossing wave period (T_z), and the peak wave period (T_p) are plotted in Figures 9 and 10. Figure 11 shows the offshore wave direction during the field experiment, measured positive clockwise from North. Corresponding cardinal points are marked for reference on the right-hand vertical axis. Longshore and cross-shore (onshore) orientations are again shown with dashed lines on the figure. The offshore wave height was in the range of 1–3 m over the course of the experiment.

5. Wind Stress Evaluation Procedure

Several methods are available for measuring the wind shear stress. Among them, the eddy correlation technique, otherwise known as the direct method, has been the most widely used wind stress measurement technique and has become the standard method in recent years. In this method, fluctuating components of horizontal and vertical wind velocities (u' and w') are measured using a fast response anemometer in order to evaluate the wind shear stress directly from $\tau = \rho_a \overline{u'w'}$. When combined with a careful quality control and necessary corrections, the eddy correlation technique provides a robust and reliable approach and was therefore used in the present field study.

The wind shear stress (τ) is evaluated based on equation (2) using the time series of the quality-controlled wind velocity measured by the ultrasonic anemometers. The averaging period for this purpose needs to be long enough to ensure that the stress-carrying scales of the turbulence can be captured and that stable results can be achieved. At the same time, the wind is rarely stationary over long periods of time. Therefore, the averaging period should also be short enough to avoid significant changes to the mean wind characteristics. The most frequent choices of the averaging period in the literature are between 15 and 30 min. An averaging period of 15 min, i.e., the duration of a data run, is used for this purpose in the present study.

The shear velocity (u_*) and the drag coefficient (C_{Dz}) are, respectively, evaluated from equations (3) and (13) once the shear stress is known. The drag coefficient is subsequently converted to the equivalent drag coefficient under neutral stability conditions. The stability parameter and therefore the buoyancy flux are required for this purpose. The sonic temperature (θ_s) recorded by ultrasonic anemometers closely approximates the virtual temperature (θ_v) and can be used for the purpose of evaluating the buoyancy flux and the stability parameter. That is, the buoyancy flux $\theta'_v w'$ can be well approximated by $\theta'_s w'$. The Monin-Obukhov length scale (L) and the stability parameter (z/L) are subsequently evaluated using equation (5). Although the temperature fluctuations (θ'_s) measured by ultrasonic anemometers are accurate for the purpose of evaluating the buoyancy flux, the measured mean temperature can be slightly offset. The anemometers, however, apply internal correction procedures to rectify this. The mean sonic temperature is also used when evaluating the Monin-Obukhov length scale from equation (5). Nevertheless, such temperature offsets do not make meaningful impacts on the evaluated L value. Once the stability parameter (z/L) is obtained, the nondimensional gradient function (ϕ_m) and the stability function (ψ_m) are readily calculated from equations (9–12). These are further used in equation (16) in order to evaluate the equivalent wind drag coefficient under neutral stability conditions (C_{DNz}). Lastly, equation (17) is used to convert C_{DNz} that is referenced to the anemometer elevation into C_{DN10} which is referenced to $z = 10$ m. The aerodynamic roughness (z_0) that is required for this purpose can be evaluated from the velocity profile in equation (6) or equation (8). In other words, knowing the shear velocity (u_*) and the measured wind speed (\bar{u}_z), the velocity profile is solved for the aerodynamic roughness.

6. Data Analysis and Quality Controls

The absence of data quality control significantly degrades the reliability of outcomes of an air-sea interaction field experiment and leads to unphysical conclusions. A series of rigorous quality control and enhancement measures have therefore been employed to ensure that measured wind stress and drag coefficients, and other conclusions from the present study are accurate and reliable. The quality control package forms an important component of the data analysis and is briefly explained here.

The first test, namely, *the rate of sampling failure*, monitors any failure to take a sample by the ultrasonic anemometers. Generally speaking, it is acceptable for data runs to contain occasional missed (failed) samples without having a meaningful impact on the evaluated turbulent fluxes. However, frequently or continuously failed samples are indicative of potential problems in the operation of anemometers, and the corresponding data records were therefore rejected. Nevertheless, most data runs contain no failed sample. For others, an evident link was found between the presence of failed samples and the rainfall intensity. This is due to rain particles momentarily blocking the path between the sonic transducers, leading to insufficient number of samples from one or more pairs of sonic transducers during a sampling attempt. It was also found typical of a wind record with a large number of failed samples to be spike-filled, in agreement with the aforementioned rain interference with sonic sampling attempts. Aylor and Ducharme [1995] have similarly reported rain effects on sonic anemometer data in the form of spikes. Therefore, the test concurrently rejected heavily spiked data records.

Sonic anemometer records can become spiky due to momentary malfunctions of electronics as well as the presence of rain droplets and other airborne particles such as the saltwater spray. The turbulent fluxes will become unreliable if spikes become excessively frequent. A *spike detection and removal procedure* was therefore employed to examine and limit the level of spikiness of ultrasonic wind records. An advanced spike detection algorithm recently developed in Schwarz [2008], based on the "Spacing Theorem," was adopted for this purpose. Data points which were detected as spikes were removed from the time series and replaced using a linear interpolation of their closest nonspike neighbors. Additionally, data records were also rejected if a large number of samples (more than 1% of the record length) were detected to be spikes or if the turbulent fluxes became largely manipulated (i.e., changed more than 5%) as the result of the despiking procedure.

The remainder of the quality control measures are nonintrusive and are performed on the despiked wind data. As a part of these measures, data runs with the mean wind speed of $\bar{u} < 3$ m/s were filtered out from the data set. Similarly, data records in which the wind was blowing from the land were also removed, with acceptable wind directions retained in the range of $50^\circ < \alpha_w < 210^\circ$ (cf., Figure 1). Additionally, nonstationary data records were also excluded from the data set. A sharp change in the mean wind speed (30% or more) or the wind direction (45° or more) between two neighboring data runs was considered to represent a nonstationary scenario. Similarly, excessive wind direction variabilities within individual data runs were also considered nonstationary cases. Accordingly, data records were taken as nonstationary if the ratio of vector-averaged to scalar-averaged wind speed fell below 0.95, as adopted in Vickers and Mahrt [1997b].

Finally, the quality-controlled wind velocity data underwent an anemometer tilt correction procedure. It is well known that an anemometer tilt relative to the vertical results in a false correlation between the measured horizontal and vertical wind velocities, and therefore an inaccurate estimate of the wind shear stress [Kraus, 1968; Deacon, 1968; Pond, 1968; Smith, 1970]. As such, it is important for the anemometer vertical axis (z), corresponding to the w component of the wind velocity to be precisely vertical. However, it is often very difficult to physically level the anemometers to the required precision. Therefore, different methods have been developed to evaluate, and subsequently rectify, anemometer tilt angles using the time series of the measured wind velocities. This includes the *Double Rotation* method [Tanner and Thurtell, 1969], the *Triple Rotation* method [McMillen, 1988], and the *Planar Fit* method [Paw U et al., 2000; Wilczak et al., 2001]. Given its advantages, the Planar Fit method was adopted in the present study to carefully evaluate and rectify anemometer tilt angles. The planar fit method was applied to all data runs with acceptable wind directions ($50^\circ < \alpha_w < 210^\circ$) that successfully passed the *rate of sampling failure* and *spikiness* quality controls. The reader is referred to Wilczak et al. [2001] for more details on the adopted tilt correction method.

A total of 1802 data runs (898 from the lower and 904 from the upper anemometer) each with the duration of 15 min passed the quality control procedures and were available for the shear stress analysis. This amounts to 450 h of quality-controlled wind data.

7. Results

7.1. Constant Shear Stress Layer

Although the wind shear stress is measured directly in the present study, it is the assumption of a constant shear stress layer that allows the measured shear stress (τ) to be taken equal to the shear stress τ_0 acting on

the ocean surface. Furthermore, the Monin-Obukhov similarity theory which is used throughout the drag coefficient idealization processes is also dependent on the assumption of a constant shear stress layer. Therefore, it is important to examine this assumption using the field measurements.

The two sonic anemometers mounted at approximately 6 and 11 m above the sand level at the wind mast location provide independent measurements of the shear stress at these two elevations. These independent observations are plotted in Figure 12 in order to examine the validity of a constant shear stress assumption. Each data point represents a 15 min long quality-controlled data run. This also applies to the remainder of figures in this paper. Note that all data runs with an offshore wind direction were filtered out by the quality control procedure. An overview of the data points suggests that they generally follow the 1:1 solid line, meaning that the assumption of a constant shear stress layer holds.

For a closer look, data points have been split into bins according to their shear stress value (τ_{11}). Each bin spans 0.025 N/m^2 . Figure 13 shows the average shear stress value of the data points within each bin. The values in the brackets are the number of data points that are used for this purpose; and the vertical bars show the standard deviation of the data. For the most part, the bin-averaged stress values from the two anemometers are very similar. It appears, though, that the shear stress at 6 m elevation becomes slightly smaller than that at 11 m for large stress values, i.e., open circles. The deviation seems to be statistically insignificant given that (a) the 1:1 line is still within the bounds of the standard deviation bars and (b) the deviation from the 1:1 line primarily takes place where the number of binned data points is small, e.g., the last three bins each contain less than 7 data points. Therefore, the evidence is not significant enough to indicate any significant systematic deviations.

7.1.1. Terrain Analysis

An internal boundary layer (IBL) forms as the wind departs the ocean and runs over the sandy beach prior to reaching the mast. The rate of IBL growth depends on the roughness of the two terrains, i.e., the surf zone and the sandy beach. For quality-controlled data runs, the shore-normal distance between the shoreline and the wind tower was in the range of 0–40 m. This figure was in fact close to zero for many data runs, such as those during high tides or high seas. Note that during the first few days of the deployment $X_{shoreline}$ was often even negative (Figure 3), but the corresponding wind speed was too low to pass the quality control. The distance over which the wind was running on the sandy beach also depends on the wind direction. Winds coming from acute angles relative to the shoreline travel longer distances on the sandy beach, while shore-normal winds do so over shorter distances.

Figure 14 shows the ratio τ_{6m}/τ_{11m} versus the distance wind was running over the sandy beach (X_{Sand}). The

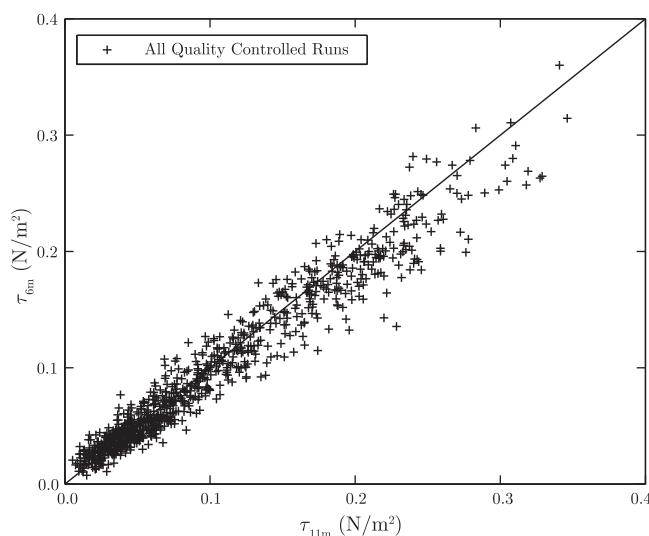


Figure 12. The shear stress measured by the lower anemometer versus that measured by the upper anemometer. The ultrasonic anemometers were mounted at approximately 6 and 11 m above the sand level. Each data point (+) represents a 15 min long data run. The solid line represents the 1:1 ratio.

measured data have been binned according to their X_{Sand} value in 10 m intervals. Note that the larger X_{Sand} values correspond to the scenarios where the wind was blowing from an acute angle relative to the shoreline, rather than very low tide conditions. Additionally, under these circumstances, X_{Sand} becomes quite sensitive to the wind direction and thus becomes unstable. For this reason and given the small number of data runs that are involved, the range of $70 \text{ m} < X_{Sand} < 100 \text{ m}$ and $X_{Sand} > 100 \text{ m}$ have each been taken as one bin. As the figure shows, the ratio of shear stresses (τ_{6m}/τ_{11m}) stays within few per cent of 1.0 when the X_{Sand} value is small. This is the case for $X_{Sand} < 50 \text{ m}$ which

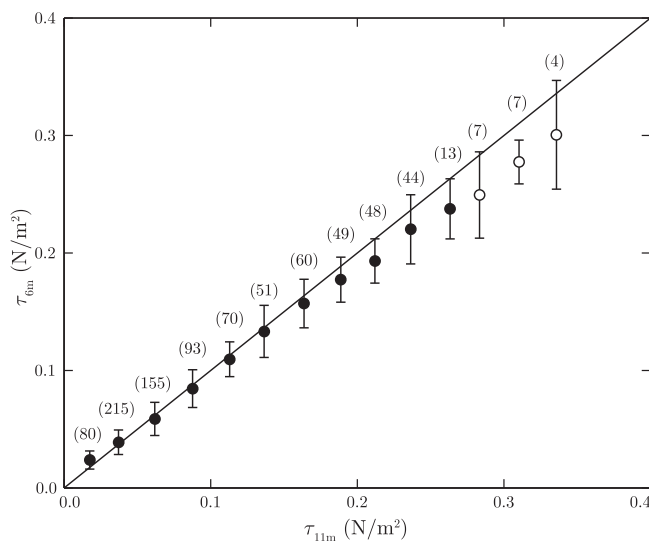


Figure 13. The shear stress measured by the lower anemometer versus that measured by the upper anemometer. The data are binned in 0.025 N/m² intervals according to their shear stress value (τ_{11m}). Filled and open circles both show the average shear stress value of the data runs within each bin. The vertical bars represent the standard deviation of τ_{6m} . The values in the brackets are the number of data points (runs) within each bin. The solid line represents the 1:1 ratio. The last three bins with the largest deviations from the 1:1 line are shown with open circles.

$X_{Sand} > 50$ m, which could be potentially affected by the IBL over the sandy beach, will be filtered out from future data analysis in order to enhance the data quality. Nevertheless, the suitable choice of the tower location has resulted in only a small number of data points being removed for this reason.

Note that the IBL refinement discussed above is not expected to specifically target the deviations from the

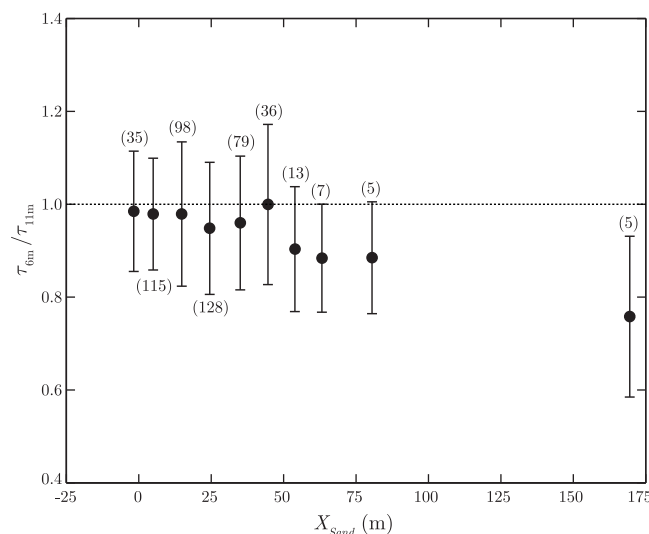


Figure 14. Ratio between the shear stresses measured at 6 and 11 m above the sand level (τ_{6m}/τ_{11m}) versus the distance the wind was running on the sandy beach (X_{Sand}). The measured data are binned according to their X_{Sand} value. The binning intervals are 10 m when $X_{Sand} \leq 70$ m. However, $70 \text{ m} < X_{Sand} < 100 \text{ m}$ and $X_{Sand} > 100 \text{ m}$ are each taken as one bin given the small number of data points falling in this range. Filled circles show the bin-averaged values. The vertical bars represent the standard deviation. The values in the brackets are the number of data points (runs) within each bin. Only quality-controlled data runs with $\tau_{11m} > 0.05 \text{ N/m}^2$ are used in order to avoid large τ_{6m}/τ_{11m} ratios prompted by near-zero τ_{11m} values.

indeed contains the bulk of the data. For larger distances ($X_{Sand} > 50$ m), the ratio appears to start deviating from 1.0. The small number of runs with large X_{Sand} values, however, makes it difficult to draw a statistically significant conclusion. With the lower anemometer being approximately 6 m above the ground, the 50 m distance corresponds to an IBL growth of 1 m in elevation for every 8 m in distance, in agreement with a detailed analysis of the IBL growth rate from a related analysis of the wind velocity profiles over $z=0.8-10$ m [Shabani, 2014]. Therefore, the choice of the tower location in the North Stradbroke 2012 field campaign appears to have successfully avoided significant IBL effects. At the same time, data points with

1:1 line for larger stress values in Figure 13. Instead, the refinement is generally concerned with the winds that are from acute angles relative to the shoreline, and/or the low tide and calm scenarios.

7.1.2. Spray Effects

Another near-boundary effect that could potentially impact the closer-to-surface measurements at the lower anemometer is salt-water spray. The last three data bins with the highest shear stress values ($\tau > 0.275 \text{ N/m}^2$) in Figure 13, shown with open circles, contain 18 data points. A second look at these data points indicate that they were collected under high wind speed conditions (12–13 m/s). In fact, these runs are from a coherent cluster of data. This raises a strong possibility of saltwater spray effects at the lower anemometer location. The

spray can affect measurements by (a) carrying parts of the shear stress and thus modifying the Reynolds stress near the surface boundary and (b) introducing measurement errors as spray (and other) particles momentarily block the path between the sonic transducers during sampling. The two effects occur at the same time, and therefore it is difficult to separate the physical effects of the spray on the Reynolds stresses from any spray-induced measurement errors. As a part of the rigorous and comprehensive quality control measures, which were applied on the present data set prior to this analysis, those records suspected of spray effects were already filtered out using the *rate of sampling failure* test. However, a small number of data runs could have slipped the quality control net. Even if this is true, the quality control protocol has still been successful, given that only a small number of runs with only marginally affected shear stress values may remain. Note that as the wind speed increases, the percentage of data runs affected by the spray also increases and so does the occasional number of data runs which may escape the controls. For instance, *Oh et al.* [2011] recently reported that 40% of their data at the wind speed of 17 m/s failed their quality control procedures. They have suggested this to be a sea-spray effect. A review of the quality control results in the present study indicates that these 18 data runs in question were indeed flagged for future attention. Additionally, they were sitting in a cluster of data where their neighbors have all been rejected, yet the data runs in question have been assigned a warning flag for their seemingly less impacted appearance. Consequently, given the potential spray impact, these 18 data runs are also filtered out. Upon removal of the spray-affected data points, as well as those with $X_{sand} > 50$ m, the best-fit line for the remaining data in Figure 13 becomes $\tau_{6m} = 0.94\tau_{11m}$ with $R^2 = 0.99$. Therefore, for the remaining data, the assumption of a constant stress layer is strongly supported by the measurements.

7.2. Atmospheric Stability

The stability parameter (z/L) represents the stability regime. In the neutral stability regime ($z/L = 0$), the vertical mixing of momentum (and other quantities) in the surface layer is entirely governed by the shear generation of the turbulence. The wind velocity profile is expected to be logarithmic under these circumstances. In a stable regime ($z/L > 0$), the thermal stratification works against the turbulence and suppresses the vertical mixing in the surface layer. The two, however, act alongside each other to enhance the overall vertical mixing in an unstable regime ($z/L < 0$). Velocity profiles will no longer be logarithmic during stable or unstable regimes given the modified vertical mixing. Instead, they are expected to follow the general form presented in equation (6). The range of $-0.1 < z/L < 0.05$ is often considered near-neutral where stability effects are still reasonably small [e.g., *Smith, 1980*].

The sonic velocity and temperature measurements were used to evaluate $\overline{u'w'}$ and $\overline{\theta'w'}$ fluxes and subsequently obtain L and z/L from equation (5). The range of z/L values is plotted in Figure 15 for both the lower and upper anemometers. The data are primarily in the near-neutral and unstable regimes. Note that the stability effects become important only at higher elevations. Around 65% of the data for the lower anemometer are within the near-neutral conditions ($-0.1 < z/L < 0.05$). At 11 m elevation, this figure is lower, with around 40% of the data being near-neutral. The remainder of the upper anemometer data are mostly limited to $z/L > -0.4$.

The stability affects the measured drag coefficient as it modifies the drag reference velocity. In order to enable a comparison between drag coefficients collected under different stability conditions, the drag coefficient is converted to the neutral-equivalent drag coefficient. The ratio between the drag coefficient (C_D) and its neutral counterpart (C_{DN}) is obtained from equation (16) and plotted versus the stability parameter in Figure 16. As shown, the extent of the impact is also dependent on the drag coefficient. The hatched area represents typical open ocean drag coefficient values, i.e., $C_{DN10} = 1 \times 10^{-3}$ to 2×10^{-3} . For these typical values and while the stability parameter is in the near-neutral range, the impact on the drag coefficient is negligible (slightly more than 5%). At $z/L = -0.4$, that is lower bound for the bulk of the upper anemometer data, the impact is about 20%. For larger drag coefficients, the impact increases further as shown in the plot.

7.3. Drag Coefficient

The neutral drag coefficients referenced to the velocity at 10 m elevation (C_{DN10}) are evaluated using the lower anemometer data and plotted in Figure 17. As noted in section 7.1, the data points potentially contaminated by the sea-spray or sand IBL effects are excluded from the figure. The horizontal axis shows $|\beta_w|$, where β_w is the angle between the "wind direction" and the "cross-shore orientation." Here $\beta_w = 0$ implies

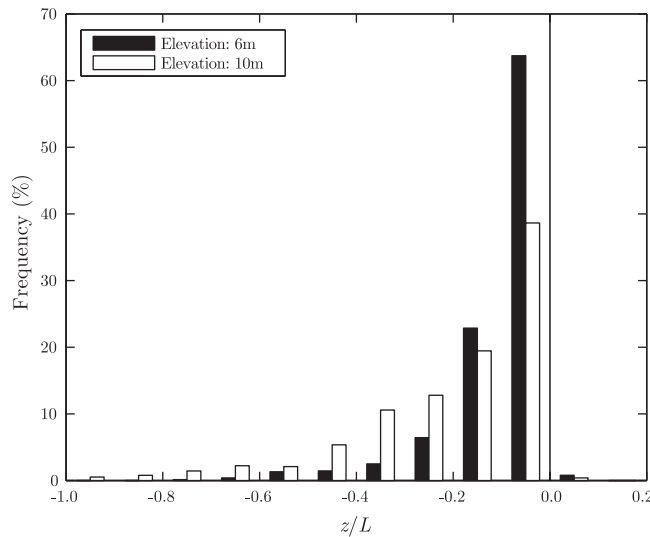


Figure 15. Distribution of the stability parameter (z/L) during the Stradbroke 2012 field campaign. The frequency refers to the percentage of quality-controlled data runs falling within corresponding z/L bins. The binning interval for the stability parameter is 0.1.

are banded according their stability condition. The data runs which are closer to the neutral stability conditions exhibit larger C_{DN10} values. The banding of the data is important since C_{DN10} is expected to be independent of the stability status. In other words, the stability effects should have been taken out once the drag coefficients (C_D) have undergone stability corrections and are reported as under neutral stability conditions (C_{DN}). The banding of the data, if not properly paid attention to, may result in misleading conclusions. Several scenarios are suggested here to explain the observed banding of the data with respect to the stability condition:

(a) *Anemometer tilt-stability interrelated effects:* As pointed out earlier, it is well known that an anemometer tilt relative to the vertical results in a false correlation between the measured horizontal and vertical wind velocities, and therefore an inaccurate estimate of the wind shear stress. It can be demonstrated that an

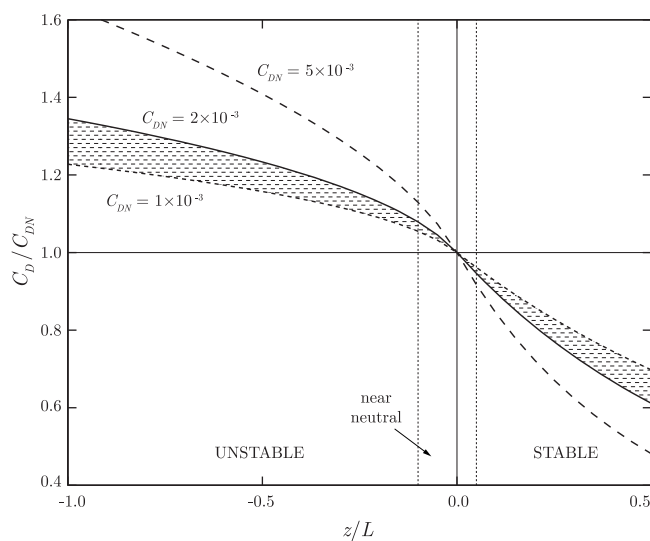


Figure 16. The ratio C_D/C_{DN} versus the stability parameter (z/L) for various C_{DN} values. The open ocean 10 m drag coefficients are typically within the hatched area between $C_{DN} = 1 \times 10^{-3}$ and 2×10^{-3} . The plot is based on the *Businger et al.* [1971] representation with numerical coefficients $\alpha_b = 20$ and $\beta_b = 5$, and the stability function as in equations (11) and (12). The dotted lines indicate the near-neutral range $-0.1 < z/L < 0.05$.

that the wind is blowing onshore and is perpendicular to the shoreline, whereas $\beta_w = \pm 90^\circ$ corresponds to when the wind is in the longshore direction. The drag coefficients are binned into four groups according to their stability length scale (L). The filled circles are those data points close to the neutral stability ($|L| \geq 100$ m). The open circles, filled triangles, and open triangles, respectively, represent more and more unstable conditions, as L approaches zero from the negative side. A similar plot has also been generated using the upper anemometer data and is shown in Figure 18.

Figures 17 and 18 indicate that the drag coefficient data (C_{DN10})

uncorrected anemometer tilt of 1° from the vertical results in approximately 6% bias in the measured wind shear stress. This estimate is applicable under neutral stability conditions. *Wilczak et al.* [2001] for instance points out that the bias rapidly climbs up to much larger values (even of the order of 100%) as the situation deviates from the neutral stability. In highly unstable conditions, in order to limit the bias to the same 6%, the tilt angle should be taken into account with an accuracy as high as 0.1° . In the present study, the Planar Fit method has been adopted during the data analysis to carefully evaluate and rectify anemometer tilt angles. An accuracy of the order of 1° , which is

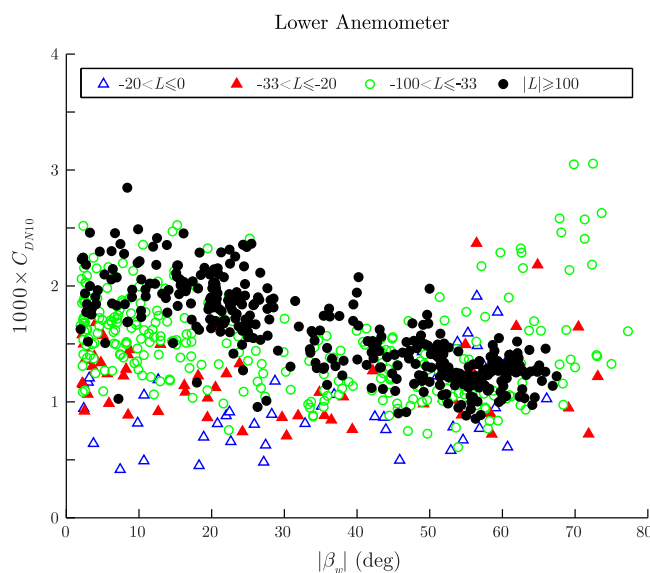


Figure 17. Neutral drag coefficient (C_{DM10}) from the lower anemometer data versus the angle (β_w) between the wind direction and the shore-normal orientation. Each data point corresponds to a 15 min data run. The data runs influenced by the sand IBL and sea-spray effects are excluded from the figure. The data runs are binned into four groups, each shown by a separate symbol, according to their stability length scale (L).

initially obtained using experiments over the land. Nevertheless, it should be acknowledged that these functions have been examined in the literature for use over the ocean as well. As such and despite some uncertainties, one can expect a good degree of confidence in the stability treatment over the ocean using these functions. A perhaps valid concern, however, is the applicability of such stability treatments for measurements at the shoreline. It is possible that complex thermal interactions at the land-sea interface cast uncertainties over both the physical meaning of thermal fluxes as well as the empirical stability functions used to address the thermal forcing. Sand IBL effects on the air-sea momentum exchange have been avoided by moving the tower very close to

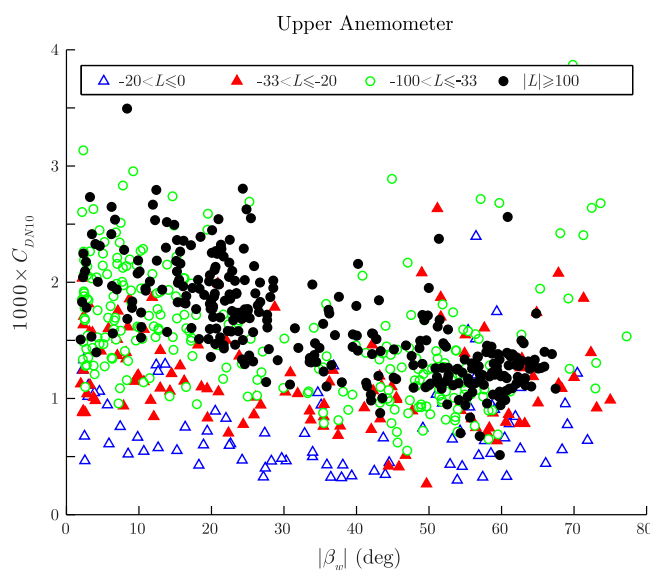


Figure 18. Neutral drag coefficient (C_{DM10}) from the upper anemometer data versus the angle (β_w) between the wind direction and the shore-normal orientation. Each data point corresponds to a 15 min data run. The data runs influenced by the sand IBL and sea-spray effects are excluded from the figure. The data runs are binned into four groups, each shown by a separate symbol, according to their stability length scale (L).

suitable for neutral stability conditions, is likely to have been achieved. However, a possible scenario could be that higher accuracies suitable for unstable conditions might have been more difficult to achieve in a field application or at least using the present setup. This may entirely or at least partially explain the banding of the measured drag coefficients with respect to the stability length scale. Any such interrelated tilt-stability effects, if applicable, are minimal for neutral data runs. Therefore, the data points under near-neutral stability conditions can continue to be confidently used.

(b) *Complex land-sea thermal interactions:* The stability functions, which are used to treat and correct the stability effects, have been initially

obtained using experiments over the land. Nevertheless, it should be acknowledged that these functions have been examined in the literature for use over the ocean as well. As such and despite some uncertainties, one can expect a good degree of confidence in the stability treatment over the ocean using these functions. A perhaps valid concern, however, is the applicability of such stability treatments for measurements at the shoreline. It is possible that complex thermal interactions at the land-sea interface cast uncertainties over both the physical meaning of thermal fluxes as well as the empirical stability functions used to address the thermal forcing. Sand IBL effects on the air-sea momentum exchange have been avoided by moving the tower very close to the shoreline, or even within the water. Alternatively, the sand IBL effects can be taken into account and rectified where the sand IBL distance is long. Likewise, one may expect a complex heat exchange pattern as the wind crosses onto the land. This may similarly need to be taken into account when treating the stability status. Both explanations, i.e., the interrelated tilt-stability effects and complex land-sea thermal interactions, promote the use of the near-neutral data at this point, given the uncertainties around unstable conditions.

In fact, it is not unprecedented to observe some significant dependence on the stability after performing the usual stability treatments. *Vickers and Mahrt [1997a]* have also reported this

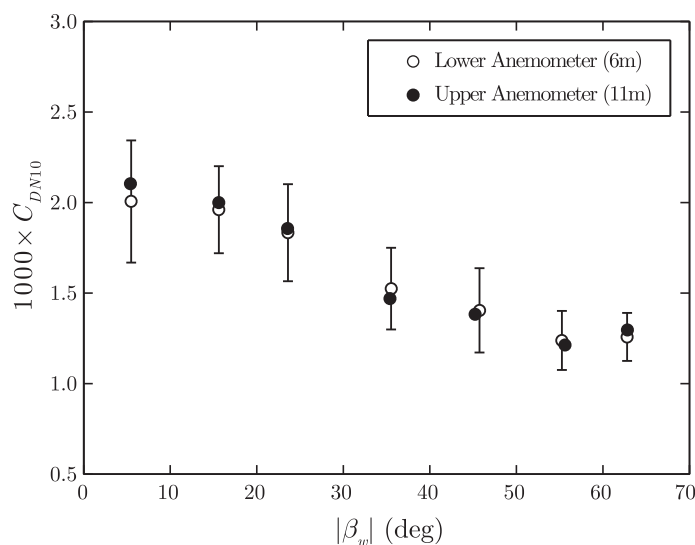


Figure 19. Variations of C_{DN10} with the angle β_w between the wind direction and the shore-normal orientation. Only the near-neutral subset of data ($|L| \geq 100$ m) are used. The data points are binned in 10° intervals according to their $|\beta_w|$ values. The filled and open circles represent the bin-averaged values for the upper and lower anemometers, respectively. The error bars represent the standard deviation for each data bin and are based on the lower anemometer data.

briefly. Their explanations were (a) possible inadequacies of the form of the stability functions and (b) large errors, not eliminated by their quality control measures, in turbulent fluxes and stability length scales during low wind speeds. Their remedy was to take data points with $|z/L| > 0.5$ out of their analysis. Some further remarks regarding the present data set may also be worth noting. Here the banding of the data points for the upper and lower anemometers is similar to each other when the data are binned according to L rather than z/L values. To demonstrate this, it can be pointed out that the overall distribution of data points in Figures 17 and 18 are the same. At the same time, the data points in both figures are also banded more or less similarly using their L values. This

would not have been the case if the binning was carried out based on z/L . It is simply because z/L values are different for lower and upper anemometers given that z is different and L is the same.

Another point worth noting is that one may argue that high wind speed data are often under neutral stability conditions, whereas low wind speed data are more often characterized by nonneutral stability conditions. It may therefore be argued on this basis that the observed banding of the data with respect to the stability is in fact a banding with respect to the wind velocity. In other words, that is to say the drag coefficient increases as the wind velocity increases. However, this is not a valid argument as will be demonstrated later. Lastly, considering only the near-neutral data points for the analysis implies that the data runs with low wind speeds will be excluded. However, the low speed runs are of little interest as far the wind forcing on the ocean is concerned.

A key aspect of Figures 17 and 18 is the variation of the drag coefficient (C_{DN10}) with the angle β_w . It can be seen within each stability group, more notably in the near-neutral data, that the drag coefficient reduces as β_w increases. In other words, onshore winds blowing perpendicular to the shoreline ($\beta_w = 0$) are characterized by the largest drag coefficients. C_{DN10} systematically drops down as the wind direction changes toward the longshore direction $|\beta_w| = 90^\circ$. The wind direction at this field site often involves a southerly component. Therefore, positive β_w values are more frequently observed. Having said, it may still be noted that the behavior of the drag coefficient versus the wind direction was found to be symmetric. That is, negative and positive β_w values are found to exhibit similar drag coefficients. Therefore, the absolute value $|\beta_w|$ has been used in the plots that are shown here.

This behavior may be explained through the concept of an *apparent wave steepness*. The water waves act as roughness elements for the overhead wind flow. As such, the drag coefficient can be expected to be associated with the wave steepness (H/λ), where H is the wave height and λ is the wave length. The wave steepness has been previously used in the parameterization of the drag coefficient and roughness in the open ocean [e.g., Hsu, 1974; Taylor and Yelland, 2001; Drennan et al., 2005]. The drag coefficient (C_{DN10}) is expected to increase as waves become steeper. Now if the wind blows with an angle relative to water waves, the wind will experience longer wave lengths as it travels from one wave crest to another when compared with the condition of wind and waves being completely aligned. The idea of an apparent wave length or subsequently an apparent wave steepness may be defined on this basis. Accordingly, as the wind changes direction from the onshore to the longshore direction, it experiences a smaller apparent wave steepness. The drag coefficient therefore reduces during longshore winds due to this reduced apparent wave steepness.

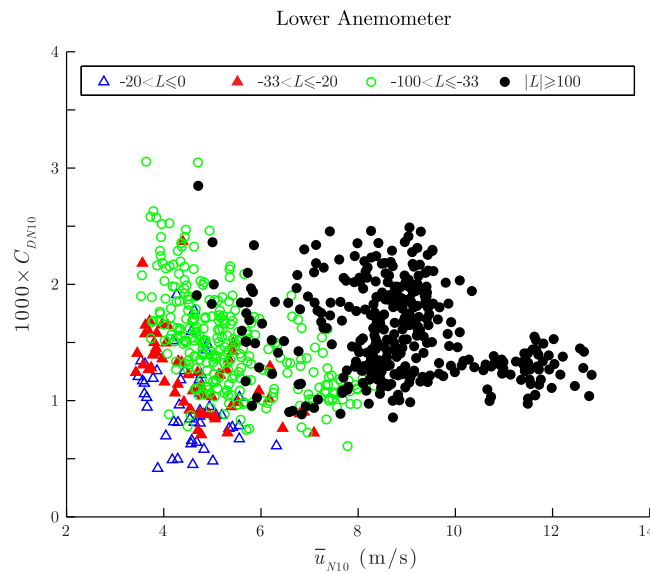


Figure 20. Neutral drag coefficient (C_{DN10}) based on the lower anemometer data versus the 10 m neutral wind speed (\bar{u}_{N10}). Each data point corresponds to a 15 min data run. The data runs influenced by the sand IBL and sea-spray effects are excluded from the figure. The data runs are binned into four groups, each shown by a separate symbol, according to their stability length scale (L).

the largest drag coefficient and therefore the strongest wind forcing on the water surface are of primary interest. Nevertheless, wind with longshore components are generally very common and also contribute to storm surge as well as the generation of wind-driven longshore currents. The latter, in combination with the Coriolis force, also generates a rise in water level along the coast for specific wind directions.

While discussing Figures 17 and 18, it was pointed out that the stability banding of the data may mistakenly be argued to be the result of C_{DN10} varying with the wind velocity. That is to say, the low wind speed range of the data is more populated by non-neutral data points, whereas the high wind speed data are mostly

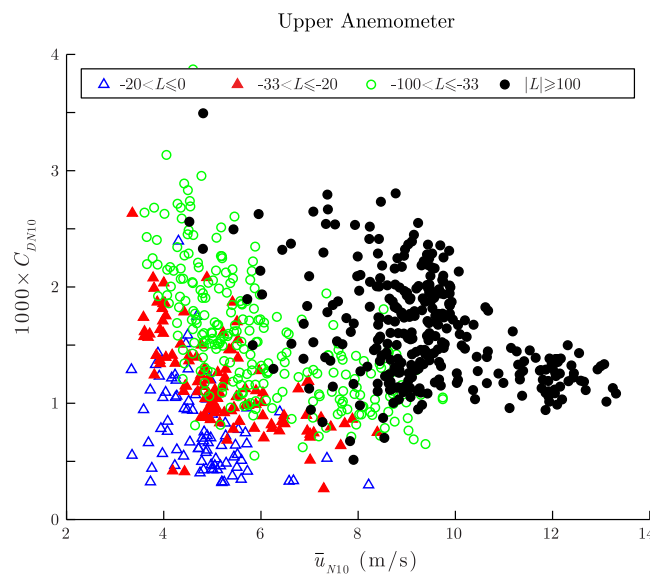


Figure 21. Neutral drag coefficient (C_{DN10}) based on the upper anemometer data versus the 10 m neutral wind speed (\bar{u}_{N10}). Each data point corresponds to a 15 min data run. The data runs influenced by the sand IBL and sea-spray effects are excluded from the figure. The data runs are binned into four groups and shown by a separate symbol, according to their stability length scale (L).

near-neutral and, hence, incorrectly argue against the stability banding of the data. Figures 20 and 21 are plotted here in order to clarify and further reject this argument and also to give a broader overview of the data set. They show the evaluated drag coefficient (C_{DN10}) versus the 10 m neutral wind velocity (\bar{u}_{N10}) using the data from the lower and upper anemometers, respectively. The data points are binned according to their stability length scale, similar to previous figures. It is evident that at any given wind velocity, the drag coefficients are still banded according to their stability length scale. Therefore, one can confidently reject the argument that the observed bandings in Figures 17 and 18 were proxies for the banding of the data with respect to the wind

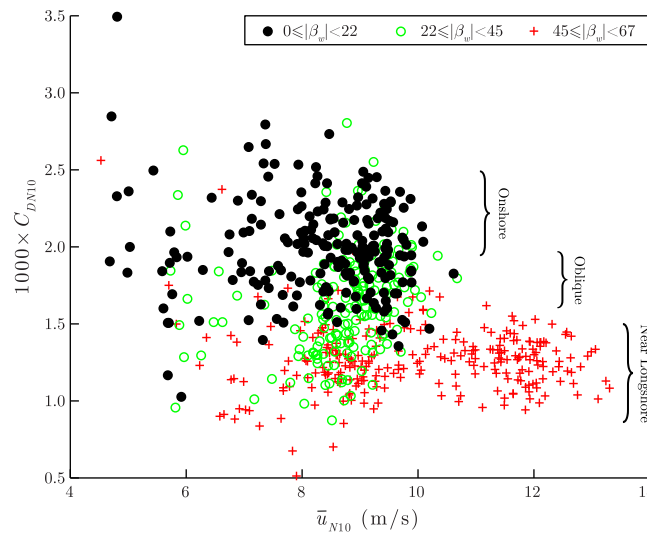


Figure 22. Neutral drag coefficient (C_{DN10}) versus the 10 m neutral wind speed (\bar{u}_{N10}). Each data point corresponds to a 15 min data run. The plot contains only near-neutral data points ($|L| \geq 100$ m). The data from both anemometers are included. The data points are binned into different groups, each shown by a separate symbol, according to their $|\beta_w|$.

and lower anemometers, i.e., the filled circles in Figures 20 and 21, have been separated and replotted in Figure 22. At the same time, these data points are now binned according to their $|\beta_w|$ value. It can be seen that the decline of C_{DN10} is evidently due the increase in $|\beta_w|$ value. The bins are qualitatively referred to as the onshore wind ($0^\circ \leq |\beta_w| < 22.5^\circ$), oblique wind ($22.5^\circ \leq |\beta_w| < 45^\circ$), near longshore wind ($45^\circ \leq |\beta_w| < 67.5^\circ$), and longshore wind ($67.5^\circ \leq |\beta_w| < 90^\circ$). A more or less similar behavior may also be observed if the other stability groups were chosen. A subset of data which is of the greatest interest in the present study is the near-neutral onshore wind data. In total, there are 244 such data points, and they will

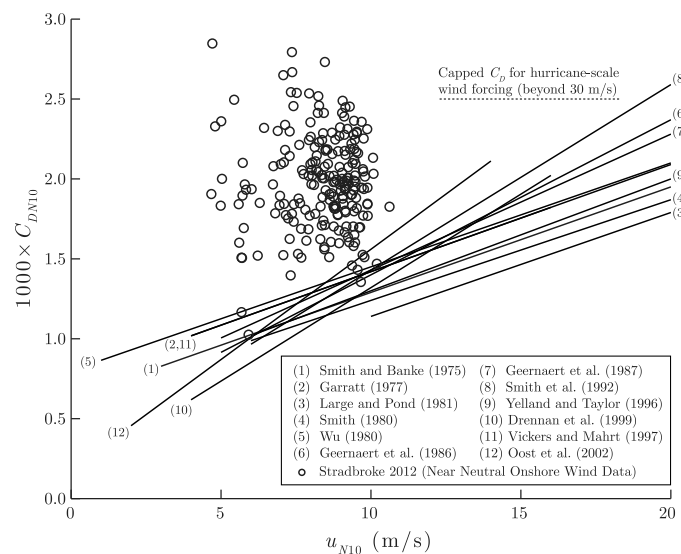


Figure 23. Comparison between neutral drag coefficients (C_{DN10}) measured over the surf zone during the Stradbroke 2012 campaign and those previously reported by other major investigations in other regions of the oceans. Near-neutral onshore wind data from both anemometers are shown for this purpose. Results of previous investigations are based on their proposed linear parameterization of the drag coefficient versus the wind speed [cf., Smith and Banke, 1975; Garratt, 1977; Large and Pond, 1981; Smith, 1980; Wu, 1980; Geernaert et al., 1986, 1987; Smith et al., 1992; Yelland and Taylor, 1996; Drennan et al., 1999; Vickers and Mahrt, 1997a; Oost et al., 2002].

form the basis for the discussion presented in the next section. It should be noted that the drag coefficient during longshore wind is still an important parameter, in particular for modeling currents.

speed. Note that, as pointed out earlier, the stability is only relevant during low wind speeds, and the data become near-neutral as the wind speed increases.

An important note regarding Figures 20 and 21 is that “the apparent decline of C_{DN10} with increasing \bar{u}_{N10} in each stability pattern and is not a real effect.” It has been mentioned earlier that the drag coefficient declines as the wind direction changes toward the longshore direction. Accordingly, there will also be a second type of banding in Figures 20 and 21 due the wind direction changes. To demonstrate this, the near-neutral data ($|L| \geq 100$ m) from both upper

and lower anemometers, i.e., the filled circles in Figures 20 and 21, have been separated and replotted in Figure 22. At the same time, these data points are now binned according to their $|\beta_w|$ value. It can be seen that the decline of C_{DN10} is evidently due the increase in $|\beta_w|$ value. The bins are qualitatively referred to as the onshore wind ($0^\circ \leq |\beta_w| < 22.5^\circ$), oblique wind ($22.5^\circ \leq |\beta_w| < 45^\circ$), near longshore wind ($45^\circ \leq |\beta_w| < 67.5^\circ$), and longshore wind ($67.5^\circ \leq |\beta_w| < 90^\circ$). A more or less similar behavior may also be observed if the other stability groups were chosen. A subset of data which is of the greatest interest in the present study is the near-neutral onshore wind data. In total, there are 244 such data points, and they will

7.4. Where Does the Surf Zone Data Stand Relative to Ocean Data?

Central to the present study is to determine how the wind stress on the surf zone compares with that previously measured in other regions, in particular the open ocean. Earlier, the “stability banding” and the “wind direction dependency” of the drag coefficient were discussed. This explains the variations in the measured drag coefficients. With this background, it is now possible to focus on the near-neutral onshore subset of the wind data

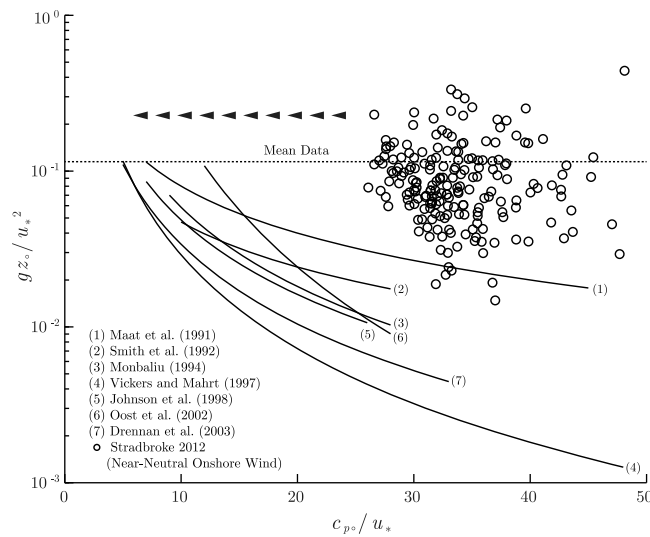


Figure 24. Comparison between the normalized aerodynamic roughness (gz_0 / u_*^2) or the Charnock coefficient measured over the surf zone during Stradbroke 2012 campaign and those previously reported by other major investigations in other regions of the oceans [cf., Maat et al., 1991; Smith et al., 1992; Monbaliu, 1994; Vickers and Mahrt, 1997a; Johnson et al., 1998; Oost et al., 2002; Drennan et al., 2003]. Near-neutral onshore wind data from both anemometers are shown for this purpose. The wave age parameter (c_p / u_*) that is used here to plot the open circles is based on the deep water wave celerity. This is evaluated using wave measurements by the Brisbane Buoy at the depth of approximately 76 m offshore the field site at North Stradbroke Island.

which is of the most interest for the present objective.

A common form of parameterization is to formulate the wind drag coefficient (C_{DN10}) as a linear function of the mean wind speed (\bar{u}_{N10}). Here a set of 12 widely cited linear drag coefficient formulations are used to compare with results of the present study. These parameterizations are plotted alongside the near-neutral onshore wind data from the present data set in Figure 23. The results of some major field campaigns such as MARSEN, HEXMAX, WAVES, SWADE, RASEX, ASGAMAGE, and others are represented by the parameterizations plotted here, including measurements in deep water, as well as data collected in shallower regions (depths of 30, 18, 15, 12, or 4 m), but all outside the surf zone.

The drag coefficients from the present data set clearly sit well above other data sets shown here. In fact, the data (open circles) yield an average drag coefficient of $C_{DN10} = 2 \times 10^{-3}$. On average and for the same wind speed, the data are characterized by drag coefficients approximately twice those over the ocean. The amount of scatter in the present data is similar to other air-sea investigations. In fact, a closer look to these data points revealed to the authors that bulk of the scatter is due to run-to-run variations of drag coefficients, rather than systematic changes. The scatter can be slightly reduced if drag coefficients from the upper and lower anemometers are averaged and plotted as a single point. This, however, does not change the conclusions drawn here and therefore is not replotted.

Another widely used type of parameterization is to express a normalized form of the sea surface roughness as a function of the wave age parameter (c_p / u_*). The aerodynamic roughness (z_0) may be normalized in different ways for this purpose. The Charnock coefficient (α) is a widely used normalized roughness

$$\alpha = \frac{gz_0}{u_*^2} \tag{19}$$

The Charnock coefficient is thought to decrease as the wave age increases. In other words, actively growing young seas display larger Charnock's coefficients than fully developed seas, and they in turn are larger than in decaying seas. The wave age dependency of the roughness is widely agreed among researchers. A common functional form for this purpose is

$$\frac{gz_0}{u_*^2} = m_1 \left(\frac{c_p}{u_*} \right)^{-n_1} \tag{20}$$

where c_p is the peak wave celerity. Existing field investigations have provided empirical values for coefficients m_1 and n_1 .

The solid curves in Figure 24 represent equation (20) using the empirical coefficients m_1 and n_1 suggested by seven previous studies in the literature. These investigations collectively contain measurements over a wide range of water depths from deep water to as shallow as 4 m. On the same graph, the onshore and near-neutral subset of the Stradbroke 2012 data from both anemometers is shown by open circles. The wave age (c_p / u_*) values that are used here to plot the data are from wave measurements by the Brisbane

Buoy located offshore the field site at the depth of 76 m. Note that the use of offshore wave celerity (c_p) data is not to imply that measured roughness values are governed by the offshore wave conditions. Instead, offshore wave data are used here to provide an estimate of the aerodynamic roughness offshore from the field site in deeper waters when seen in conjunction with the solid lines in Figure 24. Note that the Charnock coefficient values that are typically cited in the literature are between $\alpha = 0.010$ and 0.020 . This indeed belongs to fully developed seas ($25 < c_p/u_* < 30$) as can be deduced from Figure 24. The Charnock coefficients from the Stradbroke 2012 field data sit markedly above previous investigations shown by the solid lines. The average Charnock coefficient for these data is shown by a dotted line and is approximately 0.110 . This is clearly an order of magnitude (or even more) larger than open ocean estimates. The offshore wave age for the subset of Stradbroke 2012 data that is used here is mostly in the range of $25 < c_p/u_* < 35$, meaning that they are not likely to have significantly involved swell. Additionally, the angle between wind and waves is varying between 0° and 30° (the average value in the subset is approximately 15°). This implies that wind and offshore waves were in good alignment. As such, no evidence can be established to attribute these large roughness values to wind wave processes offshore of the surf zone. At the same time, an internal boundary layer (IBL) forms across the surf zone as the roughness changes from that outside the breakpoint. For the presented subset of data and typical values of the breaker index, the largest waves break at approximately 400 m distance from the shoreline, while the significant waves do so at about 300 m. An estimate of the IBL thickness [Panofsky and Townsend, 1964], using typical offshore roughness values and the observed surf zone roughness, suggests that the IBL grows to between 30 and 40 m elevation before reaching the measurement point. The 10 m high wind tower at the shoreline and the two sonic anemometers at nominal heights of 5 and 10 m are therefore well within the IBL. This is consistent with the observed constant stress layer.

From another perspective, wave age (c_p/u_*) values in the range of 0–10 are required to explain the large roughness values observed in the present study. In fact, $c_p/u_* = 6$ appears to be a good average estimate for this purpose. Arrows in Figure 24 show this concept, requiring the open circles to be shifted to the left toward much smaller wave age values in order to become explainable by the existing parameterizations. Shear velocities (u_*) in the subset of the Stradbroke 2012 data used here are mostly between 0.30 and 0.45 m/s, with an average value of $u_* = 0.37$ m/s. A celerity of $c_p = 2.2$ m/s is then needed to provide the required wave age of $c_p/u_* = 6$. According to shallow water wave theory $c = \sqrt{gh}$, such a small celerity corresponds to a water depth of merely $h = 0.5$ m. Perhaps, the most conservative estimate of h would be achieved by repeating the same approach as above while using the upper limits of u_* and c_p/u_* , namely, 0.45 m/s and 10, instead of their average estimates. This leads to $c_p = 4.5$ m/s and $h = 2$ m. This range of water depths corresponds to the inner surf zone. Consequently, wave celerity values of the order of those found in the inner surf zone are required in order to mathematically explain the observed large roughness values using existing parameterizations. However, the present argument is not in any way intended to conclude that the physics of air-sea interaction over the surf zone is the same as that over open oceans. Among other physical contexts, the wave age has been seen in previous investigations in the context of the relative velocity between wind and waves in order to take the roughness mobility into account. In that sense, c_p/u_* can be used to explain large roughness values encountered over the surf zone. Though, it is now more appropriate to refer to c_p/u_* as “the wave celerity over the wind shear velocity” given that the term “wave age” is of little relevance in the context of the surf zone. Open ocean waves propagate with much faster speeds than those found in shallow waters. Indeed, for mature seas, wind and waves travel with very close speeds to each other. This has been seen as a reason for the small roughness values observed in open oceans. Hence, a wave celerity of the order of those found in the inner surf zone can explain the roughness values measured during the Stradbroke 2012 field campaign. However, this is only one difference between surf zone and deep ocean waves. Surf zone waves are of sawtooth shape, compared with deep water waves which have a more sinusoidal shape. One can intuitively expect sawtooth waves in the surf zone to be rougher than more sinusoidal deep water waves because of flow separation over backward facing step. As such, the wind shear stress is expected to be larger over breaking waves in the surf zone. Slowly travelling waves together with sawtooth wave shapes thus explain the large drag coefficients and roughness values measured over the surf zone.

8. Summary and Conclusions

An extensive field campaign has been performed to study the wind stress over the surf zone. The eddy correlation technique was adopted for this purpose, with wind data collected using two ultrasonic high-

frequency anemometers mounted at 6 and 11 m above the base of a wind mast located in the intertidal and surf zones. A comprehensive quality assurance process was performed, including an assessment of an internal boundary layer due to terrain change. Similarly, the effect of an IBL generated by wind running over the beach upwind of the wind mast was also investigated. It was found that the sand IBL effects are important for the layer between the two anemometers only if the wind propagation distance over the beach was more than 50 m. In the present study, the base of the wind tower was mostly very close to or inside the water. A very limited number of data points, with acute wind angles relative to the shoreline, exceeded the 50 m threshold and were removed from the analysis. The assumption of a constant shear stress layer was examined by comparing the data obtained from the two anemometers and was validated, with the exception of a limited number of data runs likely contaminated by sea-spray. The present data set was mostly in near-neutral conditions, but unstable conditions (mostly $-0.4 < z/L < 0$) were also present. Drag coefficients were still banded with respect to the stability, despite conversion to neutral stability conditions. The stability banding of the data was discussed and explained based on interrelated tilt-stability effects, as well as complex land-sea thermal interactions and their influence on thermal fluxes and empirical stability functions. Only the near-neutral subset of the data set was used for the subsequent data analysis. The wind drag coefficient was found to systematically change with the wind angle of approach relative to the shoreline. The drag coefficients during longshore winds were on average $C_{DN10} = 1.25 \times 10^{-3}$ and were found to be much smaller than those during onshore winds ($C_{DN10} = 2 \times 10^{-3}$). The differences were explained based on the idea of the apparent wave steepness. The onshore near-neutral subset of the data was compared with the existing studies on the wind drag coefficient and the roughness outside the surf zone. The drag coefficients over the surf zone measured during the Stradbroke 2012 study were found to be on average $C_{DN10} = 2 \times 10^{-3}$ for $\bar{u}_{10} = 5-11$ m/s. This is almost twice the values predicted for the same wind speed by existing linear drag coefficient formulations based on observations outside the surf zone. The differences are attributed to different wave celerity and wave shapes in the nearshore region. The observed Charnock coefficient was on average 0.110 which is an order of magnitude larger than open ocean values. The results were also compared with the existing wave age-dependent parameterizations of the Charnock coefficient. It was found that a wave celerity of the order of those observed in the inner surf zone is required to explain the observed large roughness and drag coefficients in the present study using existing wave age-dependent parameterizations.

Acknowledgments

This study was sponsored by the ARC Discovery grant DP0877235 provided by the Australian Research Council. The authors would like to acknowledge the support of the Australian Bureau of Meteorology (BoM) for supplying AWS observations, the Australian Department of Science, Information Technology, Innovation and the Arts (DSITIA) for providing Brisbane wave buoy observations, Maritime Safety Queensland (MSQ) for supplying Mooloolaba tidal recordings, and Geoscience Australia for supplying GIS mapping data.

References

- Andreas, E. L. (2009), Relating the drag coefficient and the roughness length over the sea to the wavelength of the peak waves, *J. Phys. Oceanogr.*, *39*(11), 3011–3020, doi:10.1175/2009jpo4189.1.
- Andreas, E. L., L. Mahrt, and D. Vickers (2012), A new drag relation for aerodynamically rough flow over the ocean, *J. Atmos. Sci.*, *69*, 2520–2537, doi:10.1175/JAS-D-11-0312.1.
- Aylor, D. E., and K. M. Ducharme (1995), Wind fluctuations near the ground during rain, *Agric. For. Meteorol.*, *76*(1), 59–73, doi:10.1016/0168-1923(94)02211-2.
- Babanin, A. V., and V. K. Makin (2008), Effects of wind trend and gustiness on the sea drag: Lake George study, *J. Geophys. Res.*, *113*, C02015, doi:10.1029/2007JC004233.
- Black, P. G., E. A. D'Asaro, T. B. Sanford, W. M. Drennan, J. A. Zhang, J. R. French, P. P. Niiler, E. J. Terrill, and E. J. Walsh (2007), Air-sea exchange in hurricanes: Synthesis of observations from the coupled boundary layer air-sea transfer experiment, *Bull. Am. Meteorol. Soc.*, *88*(3), 357–374, doi:10.1175/bams-88-3-357.
- Businger, J. A., J. C. Wyngaard, Y. Izumi, and E. F. Bradley (1971), Flux-profile relationships in the atmospheric surface layer, *J. Atmos. Sci.*, *28*(2), 181–189, doi:10.1175/1520-0469(1971)028<0181:fprita>2.0.co;2.
- Charnock, H. (1955), Wind stress on a water surface, *Q. J. R. Meteorol. Soc.*, *81*(350), 639–640, doi:10.1002/qj.49708135027.
- Deacon, E. L. (1968), The levelling error in Reynolds stress measurement, *Bull. Am. Meteorol. Soc.*, *49*, 836.
- DeCosmo, J. (1991), Air-sea exchange of momentum, heat and water vapor over Whitecap Sea states, PhD thesis, Univ. of Washington, Seattle.
- Donelan, M. A., B. K. Haus, N. Reul, W. J. Plant, M. Stiassnie, H. C. Graber, O. B. Brown, and E. S. Saltzman (2004), On the limiting aerodynamic roughness of the ocean in very strong winds, *Geophys. Res. Lett.*, *31*, L18306, doi:10.1029/2004GL019460.
- Drennan, W. M., K. K. Kahma, and M. A. Donelan (1999), On momentum flux and velocity spectra over waves, *Boundary Layer Meteorol.*, *92*(3), 489–515, doi:10.1023/a:1002054820455.
- Drennan, W. M., H. Graber, D. Hauser, and C. Quentin (2003), On the wave age dependence of wind stress over pure wind seas, *J. Geophys. Res.*, *108*(C3), 8062, doi:10.1029/2000JC000715.
- Drennan, W. M., P. K. Taylor, and M. J. Yelland (2005), Parameterizing the sea surface roughness, *J. Phys. Oceanogr.*, *35*(5), 835–848, doi:10.1175/jpo2704.1.
- Dunn, S. L. (2003), Wave setup in river entrances, PhD thesis, Univ. of Queensland, Brisbane, Australia.
- Garratt, J. R. (1977), Review of drag coefficients over oceans and continents, *Mon. Weather Rev.*, *105*(7), 915–929, doi:10.1175/1520-0493(1977)105<0915:rodcoo>2.0.co;2.
- Geernaert, G. L., K. B. Katsaros, and K. Richter (1986), Variation of the drag coefficient and its dependence on sea state, *J. Geophys. Res.*, *91*, 7667–7679, doi:10.1029/JC091iC06p07667.

- Geernaert, G. L., S. E. Larsen, and F. Hansen (1987), Measurements of the wind stress, heat flux, and turbulence intensity during storm conditions over the North Sea, *J. Geophys. Res.*, *92*, 13,127–13,139, doi:10.1029/JC092iC12p13127.
- Hanslow, D. J., and P. Nielsen (1992), Wave setup on beaches and in river entrances, in *Proceedings of 23rd International Conference on Coastal Engineering*, pp. 240–252, edited by B. L. Edge, Coastal Eng. Res. Council, Venice, Italy, doi:10.9753/icce.v23.
- Hicks, B. B. (1972), Some evaluations of drag and bulk transfer coefficients over water bodies of different sizes, *Boundary Layer Meteorol.*, *3*(2), 201–213, doi:10.1007/bf02033919.
- Hsu, S. A. (1974), A dynamic roughness equation and its application to wind stress determination at the air-sea interface, *J. Phys. Oceanogr.*, *4*(1), 116–120, doi:10.1175/1520-0485(1974)004<0116:adreai>2.0.co;2.
- Hwang, P. A. (2004), Influence of wavelength on the parameterization of drag coefficient and surface roughness, *J. Oceanogr.*, *60*(5), 835–841, doi:10.1007/s10872-004-5776-8.
- Hwang, P. A. (2005a), Comparison of ocean surface wind stress computed with different parameterization functions of the drag coefficient, *J. Oceanogr.*, *61*(1), 91–107, doi:10.1007/s10872-005-0022-6.
- Hwang, P. A. (2005b), Drag coefficient, dynamic roughness and reference wind speed, *J. Oceanogr.*, *61*(3), 399–413, doi:10.1007/s10872-005-0050-2.
- Hwang, P. A. (2010), Comments on relating the drag coefficient and the roughness length over the sea to the wavelength of the peak waves, *J. Phys. Oceanogr.*, *40*(11), 2556–2562, doi:10.1175/2010jpo4409.1.
- Hwang, P. A., H. Garca-Nava, and F. J. Ocampo-Torres (2011), Dimensionally consistent similarity relation of ocean surface friction coefficient in mixed seas, *J. Phys. Oceanogr.*, *41*(6), 1227–1238, doi:10.1175/2011jpo4566.1.
- Jarosz, E., D. A. Mitchell, D. W. Wang, and W. J. Teague (2007), Bottom-up determination of air-sea momentum exchange under a major tropical cyclone, *Science*, *315*, 1707–1709, doi:10.1126/science.1136466.
- Johnson, H. K., J. Hojstrup, H. J. Vested, and S. E. Larsen (1998), On the dependence of sea surface roughness on wind waves, *J. Phys. Oceanogr.*, *28*(9), 1702–1716, doi:10.1175/1520-0485(1998)028<1702:otdoss>2.0.co;2.
- Kitaigorodskii, S. A., and Y. A. Volkov (1965), On the roughness parameter of the sea surface and the calculation of momentum flux in the near-water layer of the atmosphere, *Izv. Atmos. Oceanic Phys., Engl. Transl.*, *1*(9), 566–574.
- Kraus, E. B. (1968), What do we not know about the sea-surface wind stress?, *Bull. Am. Meteorol. Soc.*, *49*, 247–253.
- Large, W. G., and S. Pond (1981), Open ocean momentum flux measurements in moderate to strong winds, *J. Phys. Oceanogr.*, *11*(3), 324–336, doi:10.1175/1520-0485(1981)011<0324:oomfmi>2.0.co;2.
- Lentz, S., R. T. Guza, S. Elgar, F. Feddersen, and T. H. C. Herbers (1999), Momentum balances on the North Carolina inner shelf, *J. Geophys. Res.*, *104*, 18,205–18,226, doi:10.1029/1999JC900101.
- Letchford, C. W., and B. C. Zachry (2009), On wind, waves, and surface drag, paper presented at 5th European and African Conference on Wind Engineering, International Association for Wind Engineering (IAWE), Florence, Italy.
- Lo, A. K., and G. A. McBean (1978), On the relative errors in methods of flux calculations, *J. Appl. Meteorol.*, *17*(11), 1704–1711, doi:10.1175/1520-0450(1978)017<1704:otreim>2.0.co;2.
- Maat, N., C. Kraan, and W. A. Oost (1991), The roughness of wind waves, *Boundary Layer Meteorol.*, *54*(1), 89–103, doi:10.1007/bf00119414.
- McMillen, R. T. (1988), An eddy correlation technique with extended applicability to non-simple terrain, *Boundary Layer Meteorol.*, *43*(3), 231–245, doi:10.1007/bf00128405.
- Monbaliu, J. (1994), On the use of the Donelan wave spectral parameter as a measure for the roughness of wind waves, *Boundary Layer Meteorol.*, *67*(3), 277–291, doi:10.1007/bf00713145.
- Oh, H.-M., K.-E. Kim, K.-J. Ha, L. Mahrt, and J.-S. Shim (2011), Quality control and tilt correction effects on the turbulent fluxes observed at an ocean platform, *J. Appl. Meteorol. Climatol.*, *50*(3), 700–712, doi:10.1175/2010jamc2367.1.
- Oost, W. A., G. J. Komen, C. M. J. Jacobs, and C. Van Oort (2002), New evidence for a relation between wind stress and wave age from measurements during ASGAMAGE, *Boundary Layer Meteorol.*, *103*(3), 409–438, doi:10.1023/a:1014913624535.
- Panofsky, H. A., and A. A. Townsend (1964), Change of terrain roughness and the wind profile, *Q. J. R. Meteorol. Soc.*, *90*(384), 147–155, doi:10.1002/qj.49709038404.
- Paulson, C. A. (1970), The mathematical representation of wind speed and temperature profiles in the unstable atmospheric surface layer, *J. Appl. Meteorol.*, *9*(6), 857–861, doi:10.1175/1520-0450(1970)009<0857:tmrows>2.0.co;2.
- Paw U. K. T., D. D. Baldocchi, T. P. Meyers, and K. B. Wilson (2000), Correction of eddy-covariance measurements incorporating both advective effects and density fluxes, *Boundary Layer Meteorol.*, *97*(3), 487–511, doi:10.1023/a:1002786702909.
- Pond, S. (1968), Some effects of buoy motion on measurement of wind speed and stress, *J. Geophys. Res.*, *73*, 507–512, doi:10.1029/JB073i002p00507.
- Powell, M. D., P. J. Vickery, and T. A. Reinhold (2003), Reduced drag coefficient for high wind speeds in tropical cyclones, *Nature*, *422*(6929), 279–283, doi:10.1038/nature01481.
- Reniers, A. J. H. M., E. B. Thornton, T. P. Stanton, and J. A. Roelvink (2004), Vertical flow structure during sandy duck: Observations and modeling, *Coastal Eng.*, *51*(3), 237–260, doi:10.1016/j.coastaleng.2004.02.001.
- Schwarz, K. T. (2008), Wind dispersion of carbon dioxide leaking from underground sequestration, and outlier detection in eddy covariance data using extreme value theory, PhD thesis, Univ. of Calif., Berkeley.
- Shabani, B. (2014), Nearshore and surf zone wind stress, PhD thesis, Univ. of Queensland, Brisbane, Australia.
- Smith, S. D. (1970), Thrust-anemometer measurements of wind turbulence, Reynolds stress, and drag coefficient over the sea, *J. Geophys. Res.*, *75*, 6758–6770, doi:10.1029/JC075i033p06758.
- Smith, S. D. (1973), Thrust anemometer measurements over the sea re-examined, *Tech. Rep. BI-R-73-1*, Bedford Inst. of Oceanogr., Dartmouth, Nova Scotia, Canada.
- Smith, S. D. (1974), Eddy flux measurements over lake Ontario, *Boundary Layer Meteorol.*, *6*(1), 235–255, doi:10.1007/bf00232487.
- Smith, S. D. (1980), Wind stress and heat flux over the ocean in gale force winds, *J. Phys. Oceanogr.*, *10*(5), 709–726, doi:10.1175/1520-0485(1980)010<0709:wsahfo>2.0.co;2.
- Smith, S. D., and E. G. Banke (1975), Variation of the sea surface drag coefficient with wind speed, *Q. J. R. Meteorol. Soc.*, *101*, 665–673, doi:10.1002/qj.49710142920.
- Smith, S. D., et al. (1992), Sea surface wind stress and drag coefficients: The HEXOS results, *Boundary Layer Meteorol.*, *60*(1), 109–142, doi:10.1007/bf00122064.
- Smith, S. D., C. W. Fairall, G. L. Geernaert, and L. Hasse (1996), Air-sea fluxes: 25 years of progress, *Boundary Layer Meteorol.*, *78*(3), 247–290, doi:10.1007/bf00120938.
- Stewart, R. W. (1974), The air-sea momentum exchange, *Boundary Layer Meteorol.*, *6*(1), 151–167, doi:10.1007/bf00232481.
- Tang, Y. M., P. Holloway, and R. Grimshaw (1997), A numerical study of the storm surge generated by tropical cyclone Jane, *J. Phys. Oceanogr.*, *27*(6), 963–976, doi:10.1175/1520-0485(1997)027<0963:ansots>2.0.co;2.

- Tanner, C. B., and G. W. Thurtell (1969), Anemoclinometer measurements of Reynolds stress and heat transport in the atmospheric surface layer, *Tech. Rep. ECOM 66-G22-F*, Dep. of Soil Sci., Univ. of Wis., Madison.
- Taylor, P. K., and M. J. Yelland (2001), The dependence of sea surface roughness on the height and steepness of the waves, *J. Phys. Oceanogr.*, *31*(2), 572–590, doi:10.1175/1520-0485(2001)031<0572:tdossr>2.0.co;2.
- Vickers, D., and L. Mahrt (1997a), Fetch limited drag coefficients, *Boundary Layer Meteorol.*, *85*(1), 53–79, doi:10.1023/a:1000472623187.
- Vickers, D., and L. Mahrt (1997b), Quality control and flux sampling problems for tower and aircraft data, *J. Atmos. Oceanic Technol.*, *14*, 512–526, doi:10.1175/1520-0426(1997)014<0512:QCAFSP>2.0.CO;2.
- Vickers, D., and L. Mahrt (2010), Sea-surface roughness lengths in the midlatitude coastal zone, *Q. J. R. Meteorol. Soc.*, *136*(649), 1089–1093, doi:10.1002/qj.617.
- Walton, T. L., and R. G. Dean (2009), Landward limit of wind setup on beaches, *Ocean Eng.*, *36*(910), 763–766, doi:10.1016/j.oceaneng.2009.03.004.
- Wilczak, J. M., S. P. Oncley, and S. A. Stage (2001), Sonic anemometer tilt correction algorithms, *Boundary Layer Meteorol.*, *99*(1), 127–150, doi:10.1023/a:1018966204465.
- Wu, J. (1969), Wind stress and surface roughness at air-sea interface, *J. Geophys. Res.*, *74*, 444–455, doi:10.1029/JB074i002p00444.
- Wu, J. (1980), Wind-stress coefficients over sea surface near neutral conditions—A revisit, *J. Phys. Oceanogr.*, *10*(5), 727–740, doi:10.1175/1520-0485(1980)010<0727:wscoss>2.0.co;2.
- Yelland, M. J., and P. K. Taylor (1996), Wind stress measurements from the open ocean, *J. Phys. Oceanogr.*, *26*(4), 541–558, doi:10.1175/1520-0485(1996)026<0541:wsmfto>2.0.co;2.
- Zachry, B. C., D. Z. Letchford, D. Zuo, J. L. Schroeder, and A. B. Kennedy (2009), Surface drag coefficient behavior during hurricane Ike, paper presented at 11th Americas Conference on Wind Engineering, American Association for Wind Engineering, San Juan.